

FILE COPY

ESD ACCESSION LIST

DRI Call No. 8 3743Copy No. 1 of 2 cys.

3

Solid State Research

1975

Prepared for the Department of the Air Force
under Electronic Systems Division Contract F19628-76-C-0002 by

Lincoln Laboratory

MASSACHUSETTS INSTITUTE OF TECHNOLOGY

LEXINGTON, MASSACHUSETTS



Approved for public release; distribution unlimited.

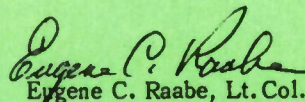
ADA 09472

The work reported in this document was performed at Lincoln Laboratory, a center for research operated by Massachusetts Institute of Technology, with the support of the Department of the Air Force under Contract F19628-76-C-0002.

This report may be reproduced to satisfy needs of U.S. Government agencies.

This technical report has been reviewed and is approved for publication.

FOR THE COMMANDER



Eugene C. Raabe, Lt. Col., USAF
Chief, ESD Lincoln Laboratory Project Office

Non-Lincoln Recipients

PLEASE DO NOT RETURN

Permission is given to destroy this document
when it is no longer needed.

MASSACHUSETTS INSTITUTE OF TECHNOLOGY
LINCOLN LABORATORY

SOLID STATE RESEARCH

QUARTERLY TECHNICAL SUMMARY REPORT
TO THE
AIR FORCE SYSTEMS COMMAND

1 MAY - 31 JULY 1975

ISSUED 22 OCTOBER 1975

Approved for public release; distribution unlimited.

LEXINGTON

MASSACHUSETTS

ABSTRACT

This report covers in detail the solid state research work of the Solid State Division at Lincoln Laboratory for the period 1 May through 31 July 1975. The topics covered are Solid State Device Research, Quantum Electronics, Materials Research, and Microelectronics. The Microsound work is sponsored by BMDATC and is reported under that program.

CONTENTS

Abstract	iii
Introduction	vii
Reports on Solid State Research	x
Organization	xiv
 1. SOLID STATE DEVICE RESEARCH	 1
A. Low-Loss High-Purity GaAs Waveguides for Monolithic Integrated Optical Circuits at GaAs Laser Wavelengths	1
B. Heterodyne Absorption Spectra of Ethylene	3
C. $\text{Pb}_{1-x}\text{Sn}_x\text{Te}$ Double-Heterostructure Diode Lasers	6
D. Long-Wavelength PbSnTe Lasers Optically Pumped with a CO_2 Laser	7
 II. QUANTUM ELECTRONICS	 11
A. $\text{NdP}_5\text{O}_{14}$ Laser Transversely Excited by a Laser Diode	11
B. Low-Threshold, CW $\text{LiNdP}_4\text{O}_{12}$ Laser	16
C. External-Cavity CO_2 -Pumped InSb Spin-Flip Laser	20
D. Optically Pumped C_2H_2 , CS_2 , and SiH_4 Lasers	24
E. Pulsed Heterodyne Measurements of Submillimeter Lasers	29
 III. MATERIALS RESEARCH	 33
A. Photoelectrolysis of Water	33
B. Crystal Structure of $\text{KNdP}_4\text{O}_{12}$	36
C. Ultrafast Growth of Thin GaAs Layers by Liquid-Phase Epitaxy	39
 IV. MICROELECTRONICS	 43
A. Charge-Coupled Imaging Arrays	43
B. Packaging Circuits for K_a -Band Parametric Amplifiers	45

INTRODUCTION

I. SOLID STATE DEVICE RESEARCH

Low-loss high-purity GaAs waveguides for monolithic integrated optical circuits have been fabricated and characterized. Attenuation measurements of waveguides at wavelengths near the GaAs absorption edge show that losses of less than 1.5 cm^{-1} at wavelengths $> 0.905 \text{ }\mu\text{m}$ can be obtained in material with $(N_D + N_A) \lesssim 2 \times 10^{15} \text{ cm}^{-3}$.

High-resolution heterodyne absorption spectra of ethylene have been determined by using the wide bandwidth and high sensitivity of recently developed HgCdTe photodiodes. With about 1 mW of CO_2 laser local-oscillator power, the signal-to-noise ratio in the 0.3- to 0.5-GHz region was better than 80:1.

Several improvements in the growth and fabrication processes used for PbSnTe double-heterostructure diode lasers have been achieved. It is anticipated that these improvements should give sufficient reproducibility to evaluate the intrinsic behavior of these devices.

CO_2 laser-pumped CW laser emission from high-quality PbSnTe crystals is reported. The optically pumped PbSnTe laser devices, which should be useful in the field of high-resolution spectroscopy, operate continuously from $16.04 \text{ }\mu\text{m}$ at liquid-helium temperature to $15 \text{ }\mu\text{m}$ at $\sim 25 \text{ K}$.

II. QUANTUM ELECTRONICS

Neodymium pentaphosphate ($\text{NdP}_5\text{O}_{14}$) has been operated quasi-CW at room temperature by transverse pumping with a laser diode emitting at $0.8 \text{ }\mu\text{m}$. The observed maximum optical-to-optical power-conversion efficiency was 7.5 percent, and the pumping threshold was 12.4 mW.

Continuous operation has been obtained in LiNd-metaphosphate ($\text{LiNdP}_4\text{O}_{12}$) using a $0.58\text{-}\mu\text{m}$ laser pump. A platelet $158 \text{ }\mu\text{m}$ thick and approximate cross section $0.5 \times 0.5 \text{ mm}^2$ was pumped normal to the platelet face, with the lasing cavity arranged collinearly to the pumping direction. The threshold power was observed to be $360 \text{ }\mu\text{W}$. For 1-mW quasi-CW operation (20-percent duty cycle), a power-conversion efficiency of 18 percent was found.

A pulsed CO_2 -pumped InSb spin-flip Raman laser has been operated with an external cavity in which the output frequency is governed to a large extent by the Fabry-Perot modes of the resonant output coupler. An output spectral width of $0.027 \pm 0.003 \text{ cm}^{-1}$ has been obtained.

Optically pumped, collisional transfer, laser action has been achieved in C_2H_2 , CS_2 , and SiH_4 . Resonant collisional transfer excites the 0100^0_0 level in C_2H_2 , a mode which is not connected to the ground state by a vibration dipole, while in

CS_2 the vibrational transfer is to the 10^0_1 combination band. In SiH_4 , in which laser operation is reported for the first time, laser output is observed at pressures up to 35 Torr.

The CW submillimeter heterodyne detection system has been extended to pulsed operation. The 8th harmonic of a klystron was mixed with pulsed far-infrared radiation from a methyl fluoride laser in a small-area GaAs Schottky diode. The CH_3F laser at $496\text{ }\mu\text{m}$, which was pumped by a CO_2 TEA laser, had a measured linewidth of less than 5 MHz.

III. MATERIALS RESEARCH

Although the internal quantum efficiency is close to 100 percent for photogalvanic cells in which a TiO_2 or SrTiO_3 anode is shorted to a platinized-Pt cathode, it has been found that because of insufficient anode band bending the maximum efficiency of photoelectrolysis with such cells is about 10 percent. For effective utilization of solar energy to generate H_2 fuel by means of photoelectrolysis, the ideal anode material should have an electron affinity no greater than $\sim 3.5\text{ eV}$ in order to achieve sufficient band bending (in addition to an energy gap $\sim 1.8\text{ eV}$).

A flux method has been used to grow crystals of $\text{KNdP}_4\text{O}_{12}$, a new, acentric, high-Nd-concentration material for use in very small, low-threshold lasers. The compound's lack of inversion symmetry may allow second-order nonlinear optical processes (e.g., second-harmonic generation) as well as linear electro-optic modulation to be carried out directly in the laser crystals.

A liquid-phase epitaxial technique has been developed for the growth of very thin GaAs layers at rates exceeding $100\text{ }\mu\text{m}/\text{min}$. By pushing a supercooled growth solution over the substrate wafer at the rate of 10 to 20 cm/sec, a reproducible thickness of about $0.1\text{ }\mu\text{m}$ has been achieved for the active layers of double-heterostructure $\text{GaAs-Ga}_{1-x}\text{Al}_x\text{As}$ diode lasers.

IV. MICROELECTRONICS

The fabrication of a two-phase, buried-channel, 100×1 charge-coupled imaging array has been completed. The device utilizes an ion-implanted barrier under alternate gates to create true two-phase operation. The channel is formed by ion-implanting phosphorous atoms, and both the first- and second-level gates are polysilicon to insure that the device has maximum sensitivity to frontside illumination. The potential well under the storage (first-level) gates at zero bias has been found to be 5.3 to 5.5 V higher than that under the transfer (second-level) gates, which agrees well with the calculated value of 5.8 V. Measurements of transfer inefficiencies have been made at a clock frequency of 1 MHz and are $1.3 \pm 0.5 \times 10^{-4}$. Lower transfer inefficiencies are expected when device processing techniques which reduce the bulk trap density in the finished devices are fully developed.

Varactor diodes are being fabricated of sufficiently high quality to be used in a K_a -band parametric amplifier for a LES-8/9 ground-station receiver. Current efforts in this program have been concentrated on developing a packaging network which provides contact between the diode and the waveguide circuit. Two packaging schemes are being evaluated to determine how each meets the electrical and mechanical requirements of the network. One approach is based on the use of a single capacitive standoff which is connected to the device by an inductive ribbon. The other approach utilizes an inductive loop and capacitive pad which are fabricated as part of the device, and these components are then connected to an external capacitive post.

REPORTS ON SOLID STATE RESEARCH

15 May through 15 August 1975

PUBLISHED REPORTS

Journal Articles

JA No.

4173	Apparent Mobility Enhancement in Inhomogeneous Crystals	C. M. Wolfe G. E. Stillman	Chapter in <u>Semiconductors and Semimetals</u> , Vol. 10, "Transport Phenomena," R. K. Willardson and A. C. Beers, Eds. (Academic Press, New York, 1975), p. 175
4393	Unified Model of the Insulator-Metal Transition in Ti_2O_3 and the High-Temperature Transitions in V_2O_3	H. J. Zeiger	Phys. Rev. B <u>11</u> , 5132 (1975)
4419	Tunable Semiconductor Diode Lasers and Applications	I. Melngailis A. Mooradian	Chapter in <u>Laser Applications to Optics and Spectroscopy</u> , S. Jacobs, M. Sargent, III, J. F. Scott, and M. O. Scully, Eds. (Addison-Wesley, Reading, Massachusetts, 1975), p. 1
4452	Planar InSb Photodiodes Fabricated by Be and Mg Ion Implantation	C. E. Hurwitz J. P. Donnelly	Solid-State Electron. <u>18</u> , 753 (1975)
4459	Screening by Fixed Charges in Compensated Semiconductors	D. M. Larsen	Phys. Rev. B <u>11</u> , 3904 (1975), DDC AD-A013947
4460	Evidence for Localized Excitations in MgO from Electron Energy-Loss Spectroscopy	V. E. Henrich G. Dresselhaus	Solid State Commun. <u>16</u> , 1117 (1975), DDC AD-A013951
4473	Low-Threshold cw $LiNdP_4O_{12}$ Laser	S. R. Chinn H. Y-P. Hong	Appl. Phys. Lett. <u>26</u> , 649 (1975)
4476	Efficient InSb Laser with Resonant Longitudinal Optical Pumping	N. Menyuk A. S. Pine A. Mooradian	IEEE J. Quantum Electron. <u>QE-11</u> , 477 (1975)
4481	Observation of a Very Narrow Surface Resonance on Single-Crystal Aluminum	V. E. Henrich	Surf. Sci. <u>49</u> , 675 (1975)
4498	PbS MIS Devices for Charge-Coupled Infrared Imaging Applications	F. J. Leonberger A. L. McWhorter T. C. Harman	Appl. Phys. Lett. <u>26</u> , 704 (1975)
4502	Crystal Structure of $NdLiP_4O_{12}$	H. Y-P. Hong	Mater. Res. Bull. <u>10</u> , 635 (1975)

JA No.

- | | | | |
|------|--|--|---|
| 4503 | Integrated GaAs-AlGaAs
Double-Heterostructure
Lasers | C. E. Hurwitz
J. A. Rossi
J. J. Hsieh
C. M. Wolfe | Appl. Phys. Lett. <u>27</u> , 241
(1975) |
| 4506 | Silicon- and Selenium-Ion-
Implanted GaAs Reproducibly
Annealed at Temperatures
Up to 950°C | J. P. Donnelly
W. T. Lindley
C. E. Hurwitz | Appl. Phys. Lett. <u>27</u> , 41
(1975) |
| 4511 | Crystallization of Amorphous
Silicon Films by Nd:YAG
Laser Heating | J. C. C. Fan
H. J. Zeiger | Appl. Phys. Lett. <u>27</u> , 224
(1975) |

Meeting SpeechesMS No.

- | | | | |
|------|---|--|--|
| 3831 | GaAs Electroabsorption
Avalanche Photodiode
Detectors | G. E. Stillman
C. M. Wolfe
J. A. Rossi
J. L. Ryan | In Gallium Arsenide and
Related Compounds (Institute
of Physics, London, 1975),
p. 210 |
| 3889 | The Gain Profile and Time-
Delay Effects in External-
Cavity-Controlled GaAs Lasers | J. A. Rossi
J. J. Hsieh
J. Heckscher | IEEE J. Quantum Electron.
<u>QE-11</u> , 538 (1975) |
| 3972 | Structure and Properties of
Magnetic Materials | J. B. Goodenough | Proceedings of Symposium on
Applied Crystal Chemistry and
Physics, <u>Transactions of the
American Crystallographic
Association</u> , Vol. 11 (American
Crystallographic Association,
New York, 1975), p. 15 |
| 3984 | Solar Energy Cooling with
Zeolites | D. I. Tchernev | Proceedings of NSF/RANN
Workshop on Solar Collectors,
New York, 21-23 November
1974, p. 262 |

* * * * *

UNPUBLISHED REPORTS

Journal ArticlesJA No.

- | | | | |
|------|---|---|--|
| 4339 | Many-Body Treatment of
Pressure Shifts Associated
with Collisional Broadening | R. W. Davies | Accepted by Phys. Rev. |
| 4469 | Low-Threshold, Transversely-
Excited NdP ₅ O ₁₄ Laser | S. R. Chinn
J. W. Pierce
H. Heckscher | Accepted by IEEE J. Quantum
Electron. |

Meeting Speeches*

MS No.

3937A	Transparent Heat Mirrors for Solar-Energy Collection	J. C. C. Fan	} 2nd Annual Symposium on Solar Energy and Its Applications, N. E. Chapter American Vacuum Society, Burlington, Massachusetts, 5-6 June 1975
4060	Photoelectrolysis of Water by Solar Energy	D. I. Tchernev	
3937B	Transparent Heat Mirrors for Solar-Energy Collection	J. C. C. Fan	Workshop - Spectrally Selective Surfaces for Photothermal Solar Energy Conversion, Minneapolis (sponsored by ERDA/NSF-RANN), 17-19 July 1975
3960	Low-Threshold, Transversely-Excited NdP ₅ O ₁₄ Laser	S. R. Chinn J. W. Pierce H. Heckscher	} 1975 IEEE/OSA Conference on Laser Engineering and Applications, Washington, D. C., 28-30 May 1975
3961	Optically Pumped Infrared Transfer Lasers	T. F. Deutsch H. Kildal	
3965	Planar HgCdTe Photodiodes for Wideband Heterodyne Detection at 10.6 μ m	D. L. Spears I. Melngailis T. C. Harman	
4070	Applications of Tunable Infrared Lasers	P. L. Kelley	
4076	Frequency Stabilization and Absolute Frequency Measurements of a cw HF/DF Laser	R. S. Eng D. L. Spears	
4077	Optically Pumped 15.90 μ m SF ₆ Laser	H. R. Fetterman H. R. Schlossberg† W. E. Barch	
3987C	GHz Bandwidth HgCdTe Photodiodes for Heterodyne Detection in the 4 to 12 μ m Region	D. L. Spears	Seminar, NASA Goddard Space Flight Center, Greenbelt, Maryland, 27 May 1975
3993	Tunable Coherent Light Sources	A. Mooradian	Conference "LASERS 75," Munich, Germany, 24 June 1975
4041	Lineshape Asymmetries in Light Scattering from Opaque Materials	A. S. Pine G. Dresselhaus	} Third International Conference on Light Scattering in Solids, Campinas, SP, Brazil, 25-30 July 1975
4099	Transient Response of an External Cavity 12 μ m Spin-Flip Laser	S. R. J. Brueck	

* Titles of Meeting Speeches are listed for information only. No copies are available for distribution.

† Author not at Lincoln Laboratory.

MS No.

4045	Energy-Loss Spectroscopy of Surface States on Titanium and Vanadium Oxides	V. E. Henrich H. J. Zeiger G. Dresselhaus	35th Annual Conference on Physical Electronics, Pennsylvania State University, University Park, Pennsylvania, 2-4 June 1975
4046	PbS MIS Devices for Charge-Coupled Infrared Imaging Applications	I. Melngailis	Infrared Detector Materials Conference, Paris, France, 26-28 May 1975
4057	Integrated GaAs-AlGaAs Double-Heterostructure Lasers	C. E. Hurwitz J. A. Rossi J. J. Hsieh C. M. Wolfe	1975 Device Research Conference, Ottawa, Canada, 24-26 June 1975
4058	Low-Loss High Purity GaAs Waveguides for Monolithic Integrated Optical Circuits at GaAs Laser Wavelengths	G. E. Stillman C. M. Wolfe J. A. Rossi H. Heckscher	
4063	Reproducible, High Carrier Concentration Implantations of Selenium and Silicon into GaAs	J. P. Donnelly W. T. Lindley C. E. Hurwitz	
4059	Photoelectrolysis of Water on Semiconducting Surfaces	D. I. Tchernev	VIII International Conference on Photochemistry, University of Alberta, Edmonton, Canada, 7-13 August 1975
4067, A, B, C	Tunable Infrared Lasers	A. Mooradian	IV Vavilov Conference on Nonlinear Optics, Novosibirsk, USSR, 12-14 June 1975; Laser Spectroscopy Conference, Megeve, France, 23-27 June 1975; Molecular Spectroscopy Conference, Erice, Italy, 28 June - 5 July 1975; Scottish University Summer School in Physics, Edinburgh, Scotland, 4-8 August 1975
4074	Application of Nonlinear Optical and High-Speed Heterodyne Techniques to Frequency Calibration in the Infrared	R. S. Eng	Thirtieth Symposium on Molecular Structure and Spectroscopy, Ohio State University, Columbus, 16-21 June 1975
4077A	Optically Pumped 15.90 μm SF_6 Laser	H. R. Fetterman H. R. Schlossberg* W. E. Barch	1975 International IEEE/APS Symposium and USNC/URSI Meeting, Urbana, Illinois, 4 June 1975

* Author not at Lincoln Laboratory.

ORGANIZATION

SOLID STATE DIVISION

A. L. McWhorter, *Head*
I. Melngailis, *Associate Head*
C. R. Grant, *Assistant*

P. E. Tannenwald
H. J. Zeiger

QUANTUM ELECTRONICS

A. Mooradian, *Leader*
P. L. Kelley, *Associate Leader*

Barch, W. E.	Heckscher, H.
Brueck, S. R. J.	Kildal, H.
Burke, J. W.	Larsen, D. M.
Chinn, S. R.	Mandel, P.*
DeFeo, W. E.	Menyuk, N.
Deutsch, T. F.	Moulton, P. F.*
Fetterman, H. R.	Parker, C. D.
Hancock, R. C.	Pine, A. S.

APPLIED PHYSICS

A. G. Foyt, *Leader*
T. C. Harman, *Assistant Leader*
C. E. Hurwitz, *Assistant Leader*

Belanger, L. J.	McBride, W. F.
Calawa, A. R.	Orphanos, W. G.
Carter, F. B.	Paladino, A. E.
DeMeo, N.	Reeder, R. E.
Donnelly, J. P.	Rossi, J. A.
Ferrante, G. A.	Spears, D. L.
Groves, S. H.	Stillman, G. E.
Krohn, L., Jr.	Walpole, J. N.
Leonberger, F. J.	

ELECTRONIC MATERIALS

J. B. Goodenough, *Leader*
A. J. Strauss, *Associate Leader*

Anderson, C. H., Jr.	Kolesar, D. F.
Animalu, A. O. E.	LaFleur, W. J.
Button, M. J.	Mastromattei, E. L.
Delaney, E. J.	Mavroides, J. G.
Dresselhaus, G.	Mroczkowski, I. H.
Dwight, K., Jr.	Oli, B.*
Fahy, R. E.	Owens, E. B.
Fan, J. C. C.	Palm, B. J.
Feldman, B.	Pantano, J. V.
Finn, M. C.	Pierce, J. W.
Henrich, V. E.	Plonko, M. C.
Hong, H. Y-P.	Reed, T. B.
Hsieh, J. J.	Tchernev, D. I.
Iseler, G. W.	Tracy, D. M.
Kafalas, J. A.	Zavracky, P. M.

MICROSOUND

E. Stern, *Leader*
R. C. Williamson, *Assistant Leader*

Alusow, J. A.	Kernan, W. C.
Brogan, W. T.	Li, R. C. M.
Cafarella, J. H.	Melngailis, J.
Dolat, V. S.	Ralston, R. W.
Efremow, N., Jr.	Smith, H. I.
Ingebrigtsen, K.	

MICROELECTRONICS

W. T. Lindley, *Leader*
F. J. Bachner, *Assistant Leader*

Beatrice, P. A.	Gray, R. V.
Bozler, C. O.	Lincoln, G. A., Jr.
Burke, B. E.	McGonagle, W. H.
Clough, T. F.	Mountain, R. W.
Cohen, R. A.	Murphy, R. A.
Durant, G. L.	Pichler, H. H.
Foley, G. H.	Smythe, D. L.
Grant, L. L.	Wilde, R. E.

* Research assistant

I. SOLID STATE DEVICE RESEARCH

A. LOW-LOSS HIGH-PURITY GaAs WAVEGUIDES FOR MONOLITHIC INTEGRATED OPTICAL CIRCUITS AT GaAs LASER WAVELENGTHS

GaAs has been investigated extensively as a material for integrated optical circuit light guides at 1.06- and 1.15- μm wavelengths. Low-loss, three-dimensional waveguides of several different types have been fabricated.¹⁻³ The change in refractive index which is responsible for the guiding action in these structures has been obtained by using either heavily doped material or a wider-bandgap material such as $\text{Al}_x\text{Ga}_{1-x}\text{As}$ as the cladding for the GaAs waveguides. Losses as low as 2 cm^{-1} also have been achieved at these wavelengths, with three-dimensional waveguides formed by using proton bombardment to decrease the carrier concentration.⁴

The main loss mechanisms at these longer wavelengths are scattering from imperfections, which can be minimized by careful materials preparation and fabrication procedures, and free carrier absorption, which can be reduced to insignificant values by using high-purity material. At shorter wavelengths, band-to-band absorption becomes important. Conceptually, it is a simple matter to use two different compositions of $\text{Al}_x\text{Ga}_{1-x}\text{As}$ to fabricate similar waveguides for shorter wavelengths, with the alloy compositions chosen to minimize band-to-band absorption and still provide the required index change for effective waveguiding. However, to effectively utilize the Franz-Keldysh electroabsorption effect for integrated modulators⁵⁻⁷ and detectors⁸ in these waveguides, it is desirable to have the sharpest absorption edge possible with minimum long-wavelength absorption tails, and to operate at a wavelength as close to the absorption edge as the losses will permit. Since the absorption tails are due to ionized impurities, they are minimal in high-purity material.

In this section, we report transmission measurements on planar high-purity GaAs light guides at wavelengths close to the band edge. These measurements indicate that low-loss guides ($\alpha \lesssim 1\text{ cm}^{-1}$) suitable for use with GaAs room-temperature lasers can be fabricated in this material. Besides simplifying the fabrication procedures for integrated optical circuits, such waveguides are well suited to the incorporation of electroabsorption modulators and detectors. If there is no "residual" absorption due to disorder in the alloy, these results can be simply extended to $\text{Al}_x\text{Ga}_{1-x}\text{As}$ waveguides.

A schematic diagram of the arrangement used to measure the waveguide transmission is shown in Fig. I-1. The source is a grating-controlled external-cavity GaAs room-temperature laser as previously described by Rossi *et al.*⁹ By adjusting the grating angle, the laser wavelength can be tuned over approximately a 150- \AA wavelength range in the vicinity of about 0.9 μm . A series of about five different laser diodes with different types of doping permits the entire wavelength range between about 0.93 and 0.85 μm or less to be covered. The external-cavity laser emission was collimated by a microscope objective, and then either directed to a spectrometer for wavelength calibration or focused on a cleaved edge of the planar waveguides for the transmission measurements. The emission from the other cleaved edge of the planar waveguides was observed with an IR microscope for alignment purposes. For quantitative transmission measurements, both the laser power incident on the cleaved edge of the waveguide and that emitted from the other cleaved edge of the waveguide were measured using a large-area Si PIN detector. Sample in-sample out transmission measurements were made on two or more different lengths of guides, and the exponential loss coefficient of the planar waveguides was calculated from the results of these measurements.

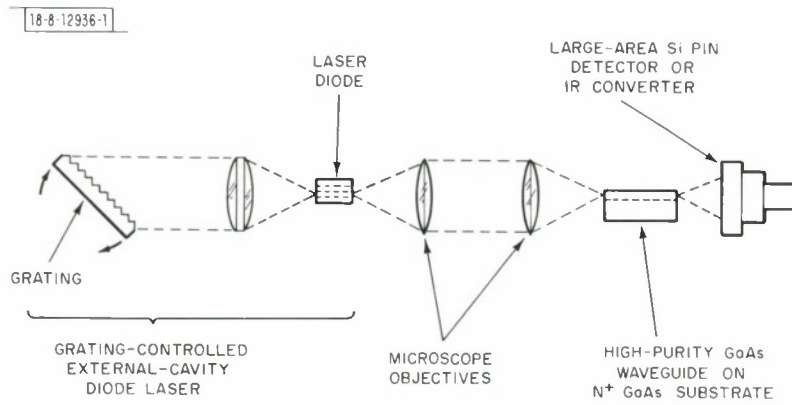


Fig. I-1. Experimental arrangement used for waveguide attenuation and electroabsorption measurements.

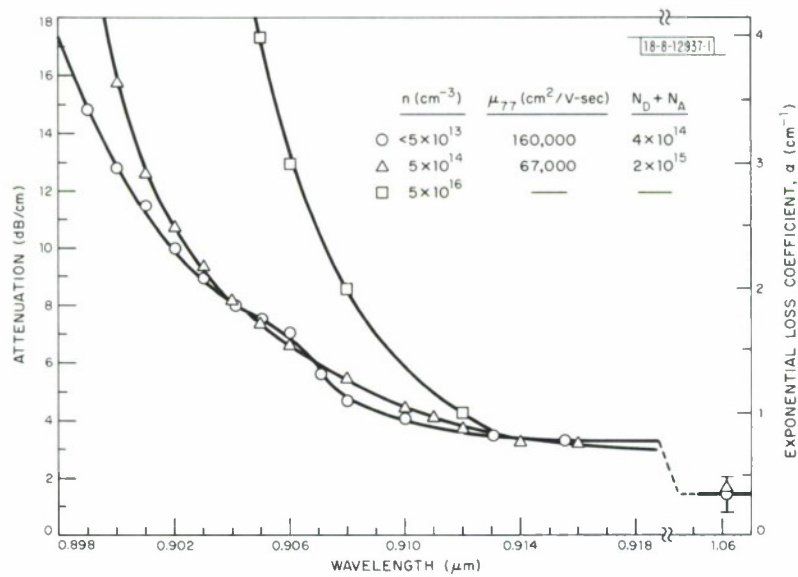


Fig. I-2. Attenuation of three different GaAs-nn⁺ waveguides close to absorption edge.

Figure I-2 shows the exponential loss coefficient variation with wavelength for three different planar GaAs waveguides. The epitaxial material for the waveguides designated by the circular and triangular data points in this figure was undoped GaAs. The epitaxial layer for the waveguides designated by the circular data points was compensated high-resistivity material with a total ionized impurity concentration estimated to be $4 \times 10^{14} \text{ cm}^{-3}$. The free carrier concentration of the epitaxial layer was $< 5 \times 10^{13} \text{ cm}^{-3}$, and the substrate carrier concentration was $1 \times 10^{18} \text{ cm}^{-3}$. The waveguide thickness was $20 \text{ }\mu\text{m}$, and this thickness and the index change due to the free-carrier effect permit the propagation of four modes higher than the lowest-order mode. The losses for the higher-order modes will be greater than that for the lowest-order mode, so that these measurements should be representative of loss coefficients that can be achieved in single-mode waveguides of the same purity. The exponential loss coefficients shown were calculated from transmission measurements on three different lengths (1.4, 0.9, and 0.5 cm) of waveguides from the same material. The error bars on the point at $1.06 \text{ }\mu\text{m}$ indicate the uncertainty in the loss coefficient α from the three different measurements. There is apparently a gradual increase in α from 0.3 cm^{-1} at $1.06 \text{ }\mu\text{m}$ to 0.7 cm^{-1} at $0.915 \text{ }\mu\text{m}$. For shorter wavelengths the increase is more rapid, reaching 0.95 cm^{-1} at $0.910 \text{ }\mu\text{m}$ and 1.5 cm^{-1} at $0.905 \text{ }\mu\text{m}$. The more rapid increase in the loss at the shorter wavelengths is due to the nearness of the absorption edge. The "tail" of the absorption at these wavelengths is presumably due to the Franz-Keldysh effect associated with the internal electric fields in the crystal that result from ionized impurities or other crystal defects,^{10, 11} although the small shoulder at $0.905 \text{ }\mu\text{m}$ for this sample must involve some other impurity absorption mechanisms. Optical absorption¹² and photoconductivity¹³ at this wavelength have been observed previously, but the defect responsible has not been identified. Also shown in Fig. I-2 (triangular data points) is the wavelength variation of the absorption coefficient determined for waveguides with epitaxial layers that have a total ionized impurity content about a factor of five greater than that for the sample previously discussed. There is very little difference in the loss coefficient for these two samples in the wavelength region of interest, and the increased absorption due to the Franz-Keldysh effect and the electric fields associated with the ionized impurities only become significant for wavelengths shorter than about $0.902 \text{ }\mu\text{m}$. It is interesting to note that there is no evidence of the absorption shoulder at $0.905 \text{ }\mu\text{m}$ for the sample. For lowest-loss waveguides in this wavelength range, it will be important to choose material in which this absorption is minimized. Figure I-2 also shows (square data points) the wavelength variation of the loss coefficient for waveguides from less-pure material. In this case the absorption in the wavelength range of interest is much higher, and waveguides from this material would not be as suitable for use for integrated electroabsorption modulators and detectors in this spectral region.

From the results presented above, it is clear that for GaAs epitaxial layers with total ionized impurity concentration ($N_D + N_A$) less than about $2 \times 10^{15} \text{ cm}^{-3}$, the planar waveguide losses are sufficiently low to permit the use and design of integrated optical circuits at wavelengths which can be achieved with GaAs heterostructure lasers. It is significant that material of this purity can be easily prepared by vapor-phase, liquid-phase, and molecular-beam epitaxial techniques.

G. E. Stillman J. A. Rossi
C. M. Wolfe H. Heckscher

B. HETERODYNE ABSORPTION SPECTRA OF ETHYLENE

High-resolution heterodyne absorption spectra of ethylene have been obtained by using the wide bandwidth and high sensitivity of recently developed HgCdTe photodiodes.¹⁴ The use of

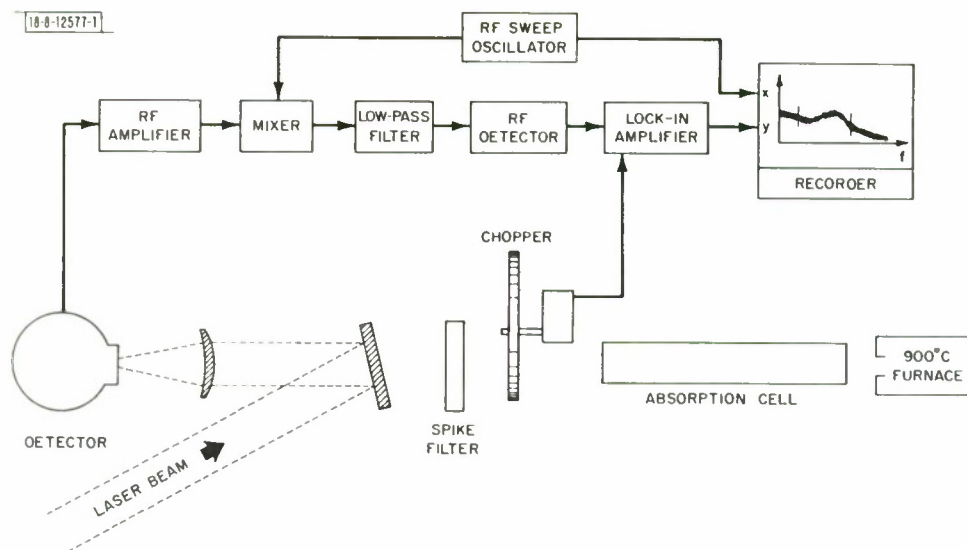


Fig. I-3. Heterodyne system for high-resolution gas absorption spectroscopy near fixed-frequency laser lines.

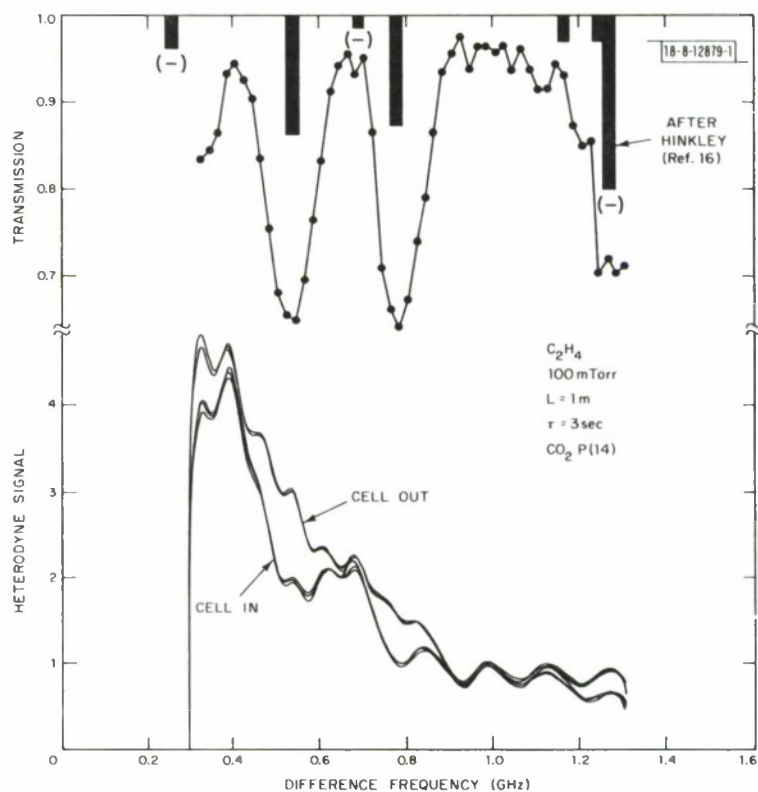


Fig. I-4. Heterodyne signal as function of IF frequency with respect to CO_2 P(14) local oscillator. Ethylene cell transmission was obtained by dividing two scans. (Fine structure is not real.)

heterodyne radiometry to detect pollutant gases has been reported;^{15,16} however, the present work is the first clearly resolved heterodyne spectra to be reported. Although direct transmission spectroscopy using tunable diode lasers is a more sensitive laboratory technique, the heterodyne technique is potentially a more versatile remote detection scheme as it offers a single-ended, passive means of detecting both stationary and moving gas sources.¹⁶

The experimental setup shown in Fig. I-3 is similar to that used previously to obtain heterodyne emission data on ethylene with a Ge (Cu) photoconductor.¹⁶ Here, the more sensitive HgCdTe photodiode was used, along with a 1-mW CO₂ laser local oscillator imaged through a 50-percent beam splitter and lens. Also in the detector's field of view was a 900°C furnace filled with a 1-inch-diameter ceramic plug. The gas absorption cell, a chopper, and a 2-percent-bandwidth spike filter which transmits only near the wavelength of the laser local oscillator, were placed between the furnace and detector. The heterodyne beat signal, generated in the detector by the laser beam and the radiation from the furnace, was amplified by a low-noise, 5- to 1500-MHz preamplifier and fed into a 10- to 3000-MHz double-balanced mixer (Vari-L Model DBM 400), where the signal was mixed with the output of a leveled sweep oscillator. The mixer output was fed into a 25-MHz low-pass filter and into a crystal square-law detector. The rectified signal was synchronously detected with respect to the chopper reference signal, integrated and displayed on the y-axis of a recorder. The x-axis was driven by the sweep output of the sweep oscillator. The recorder trace thus presented the heterodyne signal as a function of the difference frequency with respect to the laser local-oscillator frequency. The spectral resolution was set by twice the bandwidth of the low-pass filter.

IF frequency scans with and without the ethylene absorption cell are shown in Fig. I-4, using the P(14) line of the CO₂ laser. Three scans are shown for each case. To compensate for reflection losses at the cell windows, the signal was attenuated by 20 percent with the cell out. Decrease in amplifier gain and the 1-GHz RC rolloff of the detector are responsible for the large drop in signal from 0.3 to 1.3 GHz. The signal-to-noise ratio in the 0.3- to 0.5-GHz region was better than 80:1, obtained with about 1 mW of laser local-oscillator power. An additional factor-of-four improvement could have been obtained by simply changing the 50-percent beam splitter to a 90-percent beam splitter, removing the 65-percent transmitting spike filter, and antireflection-coating the absorption cell and detector dewar windows.

The transmission spectra shown in the upper half of Fig. I-4 were obtained by dividing the "cell in" signal by the "cell out" signal. (The fine structure results from connecting arbitrary sampling points and is of no significance since it falls within the range of experimental uncertainty.) The four distinct absorption lines in the Q-branch of the ν_7 vibration of ethylene are in good agreement with Hinkley's tunable diode laser transmission data.¹⁶ The minus (-) sign over some of the lines indicates that these lines are on the opposite side of the CO₂ P(14) line and have a shorter wavelength than the laser line, as determined in Ref. 16. The sign of the difference frequency cannot be determined from a single heterodyne frequency scan. However, if one were to increase the laser local-oscillator frequency by 10 or 20 MHz and repeat the spectral scan, the sign of the difference frequency for each line would be revealed by the sign of the shift in frequency of that line. The 83-MHz linewidth of the data in Fig. I-4 was due to the 66-MHz Doppler-limited linewidth as observed in diode laser transmission measurements¹⁷ and the 50-MHz detection bandwidth of the heterodyne system.

D. L. Spears

C. $\text{Pb}_{1-x}\text{Sn}_x\text{Te}$ DOUBLE-HETEROSTRUCTURE DIODE LASERS

High-performance $\text{Pb}_{1-x}\text{Sn}_x\text{Te}$ double-heterostructure (DH) diode lasers, emitting in the 10.5- μm wavelength region at 12 K, were reported previously.¹⁸ These heterostructures were grown by liquid-phase epitaxy (LPE) from metal-rich solutions on PbTe substrates which were doped with Tl in order to keep them p-type, even when metal-saturated by contact with the growth solutions. A mask of MgF_2 on the substrate permitted epitaxial growth in stripe form.

Since that time we have extended this technique to lasers with emission as far out as $\lambda \approx 20 \mu\text{m}$, using substrates of Tl-doped $\text{Pb}_{0.90}\text{Sn}_{0.10}\text{Te}$. Lattice-matched heterostructure lasers using $\text{Pb}_{1-x}\text{Sn}_x\text{Te}$ and $\text{PbTe}_{1-y}\text{Se}_y$ alloys also have been made, and we have doped the heterostructure layers during LPE growth using Bi and Tl as n- and p-type dopants, respectively. While this work has demonstrated the flexibility of the LPE double-heterostructure growth, the questions of optimum impurity doping, importance of lattice matching, and ultimate performance of the devices have gone largely unanswered because of difficulties in growth and fabrication which cause highly variable performance from device to device. We report here on progress in eliminating the sources of this variable behavior.

The most straightforward LPE growth is in planar form, but, because of spreading resistance in the passive layers of the heterostructure, deposition of a contacting stripe on the planar growth does not give a well-defined stripe-geometry laser. It is necessary to first mask and etch a mesa, then to insulate etched parts of the structure, and finally to metalize the mesa top — a process we have successfully carried out, but which has several disadvantages. One consideration is that this requires a large number of fabrication steps following growth, which makes it difficult to avoid damaging the active layer of the device. Also, forward-bias resistances of diodes made this way are typically a few tenths of an ohm, a factor of ten higher than those for diodes that have been metalized upon removal from the LPE system, without photoresist application and other processing steps.

These disadvantages of the planar growth are serious enough so that we presently favor growth in stripe form, where the application of photoresist, the etching, and the insulator deposition are done prior to growth, and only metalization, sawing, and cleaving to final size are post-growth fabrication steps. Two forms of stripe growth have been tried. In the first, there are stripe openings in the MgF_2 covering the planar substrate surface. It is necessary to briefly electropolish this structure, typically removing 1 to 2 μm of material, in order to get good wetting of the LPE growth. The growth in these shallow valleys frequently traps some growth solution, and this may cause a shunting path across the diode, a problem that has often contributed to the variable device behavior mentioned above.

A second form of stripe growth, which seems not to have this difficulty, is growth on slightly raised stripes, or mesas. Our initial procedure for fabricating the mesa substrates was first to develop a photoresist etching mask in the form of 50- μm , 4-mm stripes on the planar substrate surface using Shipley AZ 1350J resist. An etch of 2-percent Br/HBr was then used to etch mesas $\sim 5 \mu\text{m}$ high. If the substrate was rinsed with water, rather than the usual methyl alcohol, the photoresist mask remained in place. MgF_2 then was deposited on this structure and removed on the mesa tops by lifting the photoresist stripes. A brief electropolish removed 1 to 2 μm of material from the mesa tops for good LPE wetting.

We noticed that the quality of the MgF_2 growth mask following this fabrication sequence was often poor, as shown by the mask turning cloudy during the brief electropolish step or crazing

badly during the growth process and not serving to mask the growth. This poor behavior was traced to the Br/HBr etching before deposition of the MgF_2 . The problem remained when rinsing was done in methyl alcohol or in basic solutions. Auger analysis confirmed the presence of Br on the etched and thoroughly rinsed surface. On the other hand, the electropolishing was found to leave a surface to which the MgF_2 readily adhered.

Following this observation, our substrate preparation procedure was changed to include a brief electropolish (10 sec removing about 2 μm of PbTe) following the Br/HBr etch. This (or a methyl alcohol rinse after the Br/HBr etch) removes the photoresist mask. It is then necessary to reapply the mask before depositing the MgF_2 . Although these steps constitute an extended fabrication process, they take place before the epitaxial growth and give reliable results. The layer of MgF_2 , approximately 1400 Å thick, is vacuum-deposited over the time span of a minute or two onto the substrate heated to $\sim 100^\circ\text{C}$. An electron-beam gun is used to evaporate the MgF_2 source material, which is in the form of chunks (supplied as evaporative-grade MgF_2 or Irtran 1 by Eastman Kodak Co.). The MgF_2 films adhere well to the substrates and do not crack or craze during the growth and fabrication process.

Lasers made with the raised stripe substrates consistently exhibit zero-bias resistances that are high enough (>10 ohms) to indicate the absence of shunting by entrapped growth solution. Forward-bias resistances are usually 0.02 to 0.04 ohm, indicating good contacting. We feel that this procedure gives us sufficient reproducibility to evaluate the intrinsic behavior of various $\text{Pb}_{1-x}\text{Sn}_x\text{Te}$ double-heterostructure lasers, and this program is currently under way.

S. H. Groves
R. E. Reeder

D. LONG-WAVELENGTH PbSnTe LASERS OPTICALLY PUMPED WITH A CO_2 LASER

Low threshold powers and CW operation in the 10- to 11- μm range for $\text{Pb}_{1-x}\text{Sn}_x\text{Te}$ lasers at 4.2 K optically pumped using a GaAs diode laser source were reported previously.¹⁹ Also, CW operation¹⁹ at 12.4- μm wavelength was observed in a 150- μm -thick etch-polished $\text{Pb}_{0.8}\text{Sn}_{0.2}\text{Te}$ sample for an incident CO_2 laser power of 350 mW. Here, optically pumped PbSnTe devices are reported which are of sufficient quality to be useful in the field of high-resolution spectroscopy in the 15- to 16- μm region.

The $\text{Pb}_{0.788}\text{Sn}_{0.212}\text{Te}$ crystals were grown from the vapor in the shape of needles using a modification of a closed-tube technique.²⁰ The specially cooled, as-grown crystals with typical dimensions of 0.18-mm thickness, 0.36-mm width, and 3-mm length are p-type at the growth temperature. The rectangular parallelepiped-shaped needles were diffused n-type by isothermally annealing the crystals at 400°C in a horizontal furnace in the unopened crystal growth ampoule and in the presence of metal-rich source material. The needle-shaped as-grown crystals were cleaved at the end in contact with the source material and mounted with vacuum grease onto a copper heat sink. The samples used had as-grown (100) faces, and the laser cavity consisted of two as-grown (100) faces which were perpendicular to the pumped surface. The incident 10.6- μm CO_2 laser pump beam was focused to a spot with a minimum beam diameter of 260 μm .

Continuous wave operation was observed from 16.04 μm at liquid-helium temperature to 15 μm at ~ 25 K, giving a temperature tuning of 1.04 μm over the region of CW operation. The CO_2 laser energy not optically converted to long-wavelength laser energy was used to produce the temperature tuning. As shown in Figs. 1-5(a) and (b), typical mode structures for the CW PbSnTe devices are dominated by one strong mode. Figure 1-6 indicates the variation in the

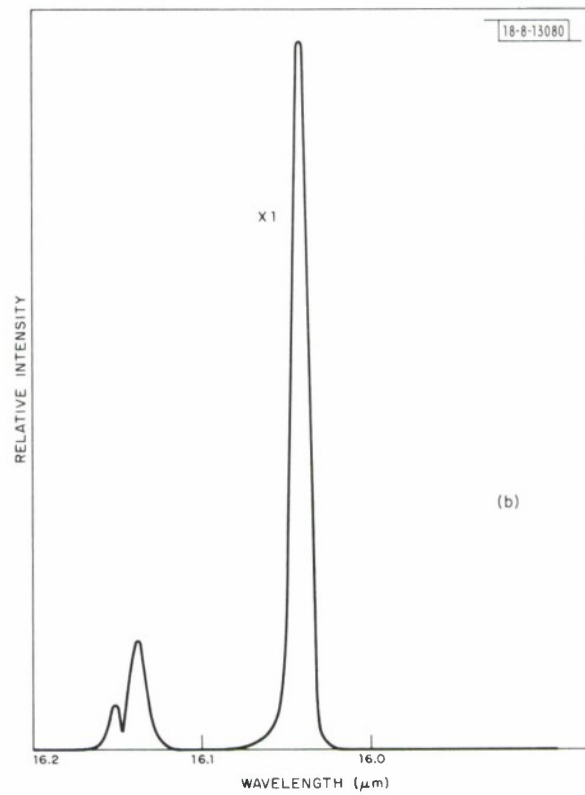
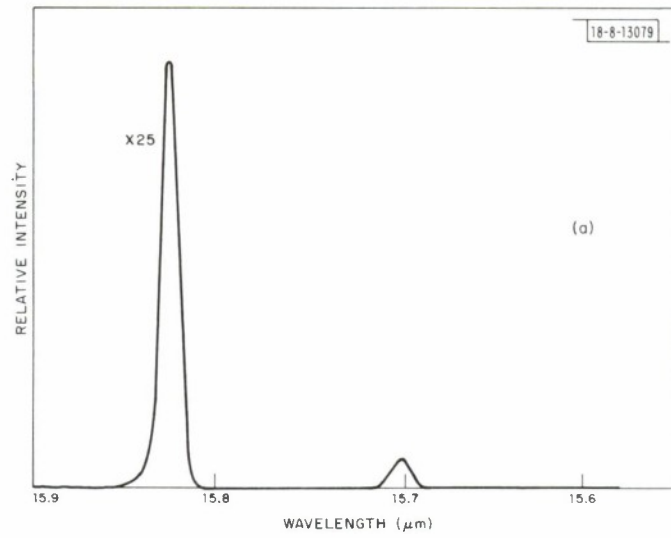


Fig. I-5. Emission spectra of CW $\text{Pb}_{0.788}\text{Sn}_{0.212}\text{Te}$ optically pumped laser: incident CO_2 power of (a) 62.5 mW and (b) 10 mW.

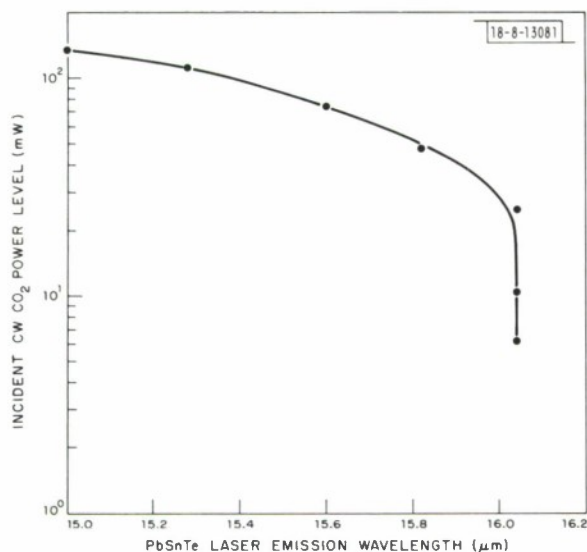


Fig. I-6. Wavelength tuning characteristic of dominant mode of optically pumped CW $\text{Pb}_{0.788}\text{Sn}_{0.212}\text{Te}$ device for various incident CO_2 power levels. Smooth curve is drawn through experimental points, which are denoted by solid circles. However, actual detailed experimental curve would be quasi-continuous due to mode hopping.

CW PbSnTe emission wavelength as the incident CO_2 laser power varied from 6.3 to 135 mW. The CW threshold for the lasing region with a 360- μm -long cavity was 6.3 mW. Taking into account reflection from the PbSnTe surface (approximately 50 percent), the equivalent PbSnTe diode threshold current density near 8 K corresponds to about 50 A/cm^2 . For a CO_2 incident power level of 135 mW, a total single-ended output power of over 0.15 mW was measured directly by a calibrated Eppley thermopile for the optically pumped PbSnTe crystal. An external quantum efficiency (assuming equal power out from both ends of the laser) of approximately 1 percent is calculated after taking into account reflection losses from the PbSnTe surface (50 percent), losses in the KRS-5 output optics window (25 percent), and absorption-reflection losses in the output optics filter (33 percent).

T. C. Harman
N. L. DeMeo

REFERENCES

1. J. C. Tracy, W. Wiegman, R. A. Logan, and F. K. Reinhart, Appl. Phys. Lett. 22, 511 (1973).
2. F. K. Reinhart, R. A. Logan, and T. P. Lee, Appl. Phys. Lett. 24, 270 (1974).
3. F. A. Blum, D. W. Shaw, and W. C. Holton, Appl. Phys. Lett. 25, 116 (1974).
4. E. Garmire, H. Stoll, A. Yariv, and R. G. Hunsperger, Appl. Phys. Lett. 21, 87 (1972).
5. F. K. Reinhart, Appl. Phys. Lett. 22, 372 (1973).
6. J. C. Dymant, F. P. Kapron, and A. J. SpringThorpe, in Gallium Arsenide and Related Compounds (Institute of Physics, London, 1975), p. 200.
7. N. Bottka and L. D. Hutcheson, J. Appl. Phys. 46, 2645 (1975).
8. G. E. Stillman, C. M. Wolfe, J. A. Rossi, and J. P. Donnelly, Appl. Phys. Lett. 25, 671 (1974), DDC AD-A006705/8.
9. J. A. Rossi, S. R. Chinn, and H. Heckscher, Appl. Phys. Lett. 23, 25 (1973), DDC AD-771902/4.
10. D. Redfield, Phys. Rev. 130, 916 (1963).
11. G. E. Stillman, D. M. Larsen, and C. M. Wolfe, Phys. Rev. Lett. 27, 989 (1971), DDC AD-737156.
12. D. Bois, J. de Physique 35, C3-241 (1974).
13. G. E. Stillman, C. M. Wolfe, J. A. Rossi, and J. L. Ryan, in Gallium Arsenide and Related Compounds (Institute of Physics, London, 1975), p. 210.
14. Solid State Research Report, Lincoln Laboratory, M.I.T. (1974:4), p. 5, DDC AD-A004763/9.
15. E. D. Hinkley, "Development and Application of Tunable Diode Lasers to the Detection and Quantitative Evaluation of Pollutant Gases," Final Technical Report to the Environmental Protection Agency, Lincoln Laboratory, M.I.T. (31 March 1972).
16. E. D. Hinkley and P. L. Kelley, Science 171, 635 (1971), DDC AD-723786; R. T. Menzies and M. S. Shumate, Science 184, 570 (1974).
17. Optics Research Reports, Lincoln Laboratory, M.I.T. (1970:2), p. 1, DDC AD-874669, and (1970:3), p. 40, DDC AD-882617.
18. S. H. Groves, K. W. Nill, and A. J. Strauss, Appl. Phys. Lett. 25, 331 (1974), DDC AD-A002773/0; Solid State Research Report, Lincoln Laboratory, M.I.T. (1974:2), p. 27, DDC AD-783634/9.
19. Solid State Research Report, Lincoln Laboratory, M.I.T. (1973:1), p. 4, DDC AD-760815; also see T. C. Harman and I. Melngailis, in Applied Solid State Science, Vol. 4, R. Wolfe, Ed. (Academic Press, New York, 1974), p. 77.
20. T. C. Harman and J. P. McVittie, J. Electron. Mater. 3, 843 (1974), DDC AD-A006315/6.

II. QUANTUM ELECTRONICS

A. $\text{NdP}_5\text{O}_{14}$ LASER TRANSVERSELY EXCITED BY A LASER DIODE

In a previous report,¹ we discussed experimental and theoretical results for $\text{NdP}_5\text{O}_{14}$ lasers transversely excited by a dye laser tuned to the $0.58\text{-}\mu\text{m}$ Nd^{3+} absorption band. We have extended that work and obtained room-temperature, quasi-CW lasing in $\text{NdP}_5\text{O}_{14}$ (NdPP) using transverse excitation from a single laser diode emitting at $0.8\text{ }\mu\text{m}$, another strong Nd^{3+} absorption wavelength.

Some slight modifications from the experimental arrangement described earlier¹ were required by the properties of the diode that was available. This double-heterostructure $\text{Al}_x\text{Ga}_{1-x}\text{As}$ diode (provided by I. Ladany of RCA), $386\text{ }\mu\text{m}$ long $\times 100\text{ }\mu\text{m}$ wide, had a room-temperature emission wavelength of $0.82\text{ }\mu\text{m}$, which required that it be cooled to increase its energy gap and shorten the wavelength to $0.80\text{ }\mu\text{m}$. This was accomplished by mounting it on the cold finger of a liquid-nitrogen dewar. A spacer inserted in the cold-finger mount reduced the thermal contact of the diode with the nitrogen reservoir, and a heater element allowed some variation of the diode temperature, so that the emission could be tuned to $0.80\text{ }\mu\text{m}$. The temperature of the diode mount for $0.80\text{-}\mu\text{m}$ emission is estimated to be in the range 210 to 240 K. The spectral output of the cooled diode is shown in Fig. II-1. To avoid damaging the diode, and to minimize the heating variation which would occur with different diode currents, the diode was driven with $300\text{-}\mu\text{sec}$ current pulses through a 50-ohm load, which matched the impedance of the pulse generator. This pulse duration was sufficiently longer than the NdPP lifetime, $115\text{ }\mu\text{sec}$, to reach the CW regime of laser oscillation. The diode and NdPP laser arrangement are shown schematically in Fig. II-2.

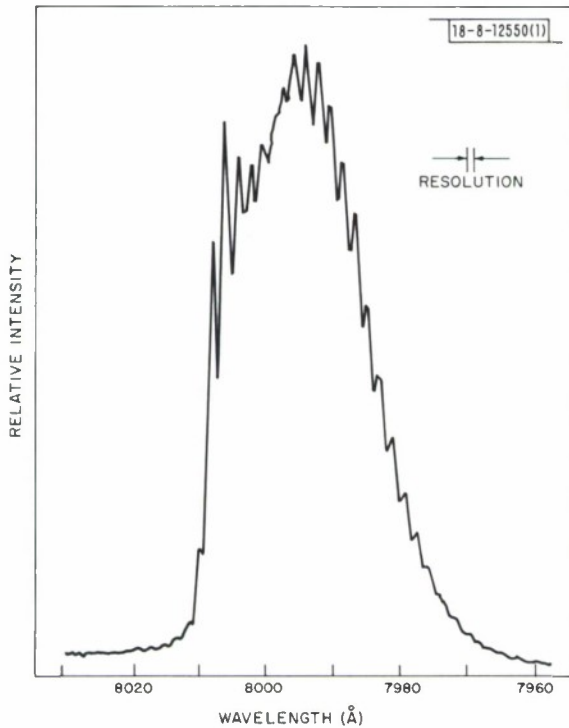


Fig. II-1. Output power as function of wavelength for cooled $\text{Al}_x\text{Ga}_{1-x}\text{As}$ pump laser diode.

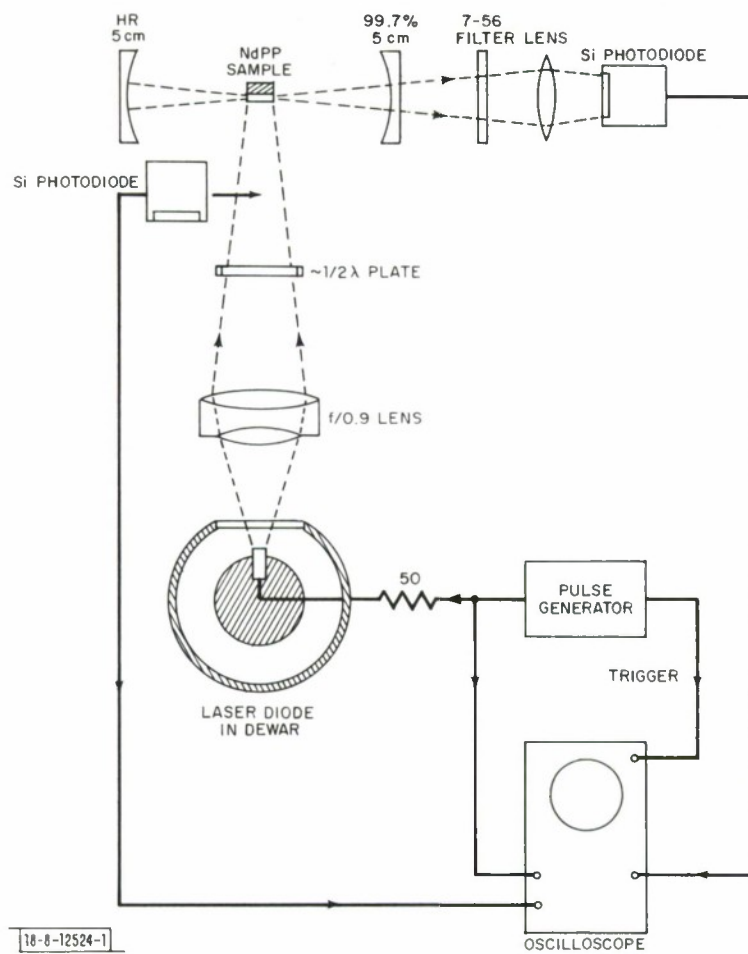


Fig.II-2. Schematic diagram of experimental apparatus for diode-pumped NdPP laser.

Another modification from the previous apparatus was in the pump collection optics. A single $f/0.9$ photographic lens imaged the narrow laser diode junction onto the NdPP sample with a magnification factor of about 3. The resulting image covered only about one-half the sample length. More significantly, the image of the NdPP fluorescence at the pump focus, viewed through a microscope with a near-infrared image converter, was not nearly as sharp as that from the transverse dye laser excitation. This is probably due to the divergent multimode output of the diode and aberration from the collection lens. This problem should be reduced in the contact geometry, which could be used with a laser diode emitting at $0.80\text{ }\mu\text{m}$ at room temperature.

Another difference from the initial experiments was in the polarization of the diode radiation, which was predominantly horizontal (TE) rather than vertical, for the dye laser. Since the NdPP absorption for the horizontal polarization was somewhat less than for the vertical, a partial half-wave plate (one designed for a different wavelength) was inserted to give approximately 60-percent conversion to vertical polarization. A 15-percent reduction in the threshold was observed, and the waveplate was retained for all lasing measurements.

These measurements were taken for two samples, both of which had lased with the transverse dye laser excitation. For one sample with $0.80\text{-}\mu\text{m}$ diode excitation, the measured optical threshold power was 12.4 mW. This is approximately 2.5 times the threshold predicted from our earlier calculations.¹ The higher-than-predicted threshold is most probably due to the poor imaging of the diode junction, as observed through an infrared microscope. No bandwidth-caused increase in threshold is expected, since the $25\text{-}\text{\AA}$ width of the diode output represents no significant increase over that of the dye laser for pumping purposes.

The maximum power-conversion efficiency for this sample was 7.5 percent, with 3.4-mW (quasi-CW) output. At the highest output levels, the power was maximized by an adjustment of the focusing lens and sample that probably caused multimode operation, as indicated by more slowly damped and noisy relaxation oscillations.

To lower the threshold by causing better absorption of the pump radiation, we polished another sample to a thickness of $78\text{ }\mu\text{m}$ and mounted it on a mirror slightly narrower than the sample length, $L = 565\text{ }\mu\text{m}$. The mirror reflected back into the sample any of the pump radiation initially transmitted through the $78\text{-}\mu\text{m}$ thickness. By using the dye laser pump, the sample had approximately the same collinear threshold ($630\text{ }\mu\text{W}$) as the previous one ($600\text{ }\mu\text{W}$), but its transverse threshold was 2.7 mW, compared with 4.0 mW. With the transverse diode excitation, the threshold was reduced from 12.4 mW for the first sample to 7.2 mW for the polished sample.

Some typical oscilloscope traces of the NdPP laser output from the second sample are shown in Figs. 11-3 and 11-4, obtained respectively at low output with clearly defined relaxation oscillations and at higher drive levels with more incoherent oscillation and evidence of multimode behavior. The output power for this sample is plotted as a function of input optical power in Fig. 11-5. The optical power-conversion efficiency reaches a maximum value of 6.7 percent. The diode efficiency can be estimated by assuming a 1.5-V drop across the diode, and computing the electrical input power from the current through the 50-ohm series load resistance. At the highest measured drive level, the diode efficiency was ~ 4.5 percent. This value represents conversion of electrical power to optical pump power actually measured at the pump focus. No correction has been made for additional losses, including vignetting and reflection by the dewar and collection lens.

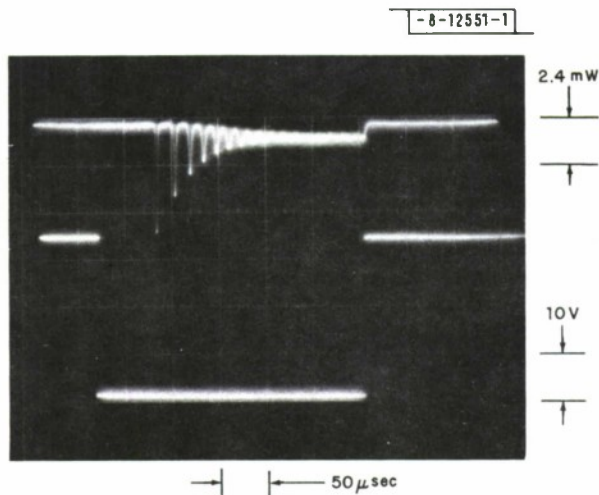


Fig.II-3. Oscilloscope trace of NdPP laser (sample 2) output and pump diode drive voltage. NdPP laser is driven ~ 4.5 times threshold, and is detuned slightly to obtain most stable relaxation oscillations. Top: NdPP output power; bottom: drive voltage - diode and 50-ohm load.

Fig.II-4. Oscilloscope trace of diode-pumped NdPP laser (sample 2), ~ 8 times threshold. Top: NdPP output power; bottom: drive voltage - diode and 50-ohm load.

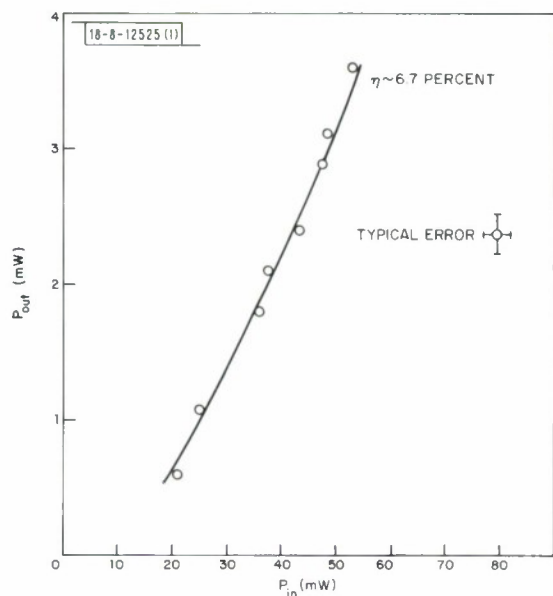
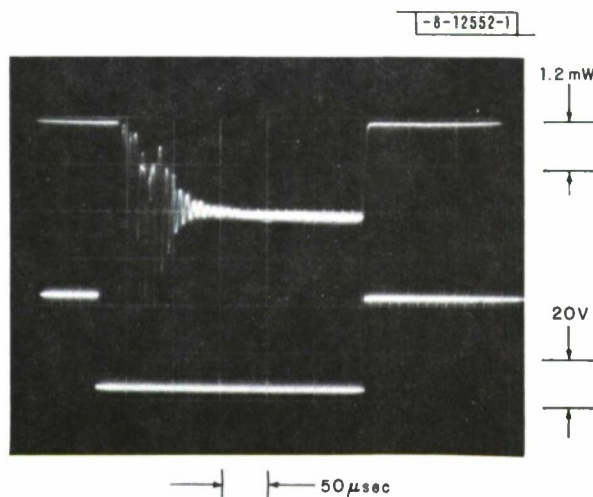


Fig. II-5. Optical output power from NdPP laser (sample 2) as function of optical input power from pump laser diode.

Finally, additional confirmation of the wavelength dependence of the threshold power was found by reducing the heating of the diode mount to obtain 0.7925- μm output. The threshold at this wavelength was 7.9 mW, only slightly higher than the 7.2-mW threshold at the maximum absorption 75 Å away.

The above theoretical and experimental results have shown clearly the feasibility of constructing miniature NdPP laser devices pumped by diodes in a simple excitation configuration without the need for elaborate sample mounts or elliptical pump reflectors. There are several reasons why such optical conversion might be desirable:

- (1) The narrow bandwidth ($\lesssim 1$ Å) of the 1.05- μm NdPP laser compared with the 20- to 50-Å bandwidth of a semiconductor laser or 300-Å bandwidth of a LED might be advantageous. For example, it would be beneficial in high-speed fiber-optic transmission systems where spectral dispersion would increase the duration of a wide-bandwidth short pulse, or in the detection of weak laser signals where optical filtering could eliminate wideband background radiation but transmit the narrow spectrum of the laser.
- (2) The mode quality and brightness of the NdPP laser should be better than that in LEDs or laser diodes, since one has more control of the laser mode in the NdPP crystal by means of the cavity reflectors. This is an important factor either in free-space transmission of low-divergence laser beams or in coupling efficiently into small-area, low-order optical fibers.
- (3) The transverse-excitation configuration itself also has advantageous features. With linear side-pumping, it should be possible to scale up the output power by increasing the number of pump diodes in the transverse array (subject, of course, to the limitations of NdPP sample length). This causes an increase in laser brightness as well as power, which is not the case when power from a multidiode source is increased by adding more diodes. A drawback to the miniature end-pumped configuration which has been employed for Nd:silica (Ref. 2) and Nd:YAG (Ref. 3) fiber lasers is that a single high-brightness source is necessary to couple efficiently into the small end area of a fiber laser. For the slightly larger LED-end-pumped polished Nd:YAG laser,⁴ the output also is limited by the power available from the single pump source.

From the present experimental results, we can estimate the amount of output power which could be obtained by using a linear array of room-temperature pump diodes. These diodes could be either high-radiance $\text{Al}_x\text{Ga}_{1-x}\text{As}$ LEDs⁵ (active region thickness ~ 2 μm , output power of 3 mW for a 50- μm -wide device) or double-heterostructure $\text{Al}_x\text{Ga}_{1-x}\text{As}$ lasers⁶ (active region thickness ~ 0.3 μm , output power of 10 mW for a 13- μm -wide device). Assume a thin NdPP sample 760 μm long having a reflecting back surface; with a spacing between stripe-geometry devices equal to the stripe width, an array of 8 LEDs or 30 lasers could be contacted to the NdPP laser crystal edge. The LED array would provide 24 mW, about 1.5 times threshold, and would be a low-power device but have the advantage of incoherent LED excitation with possibly

greater reliability than that of laser diodes. The laser-diode configuration would provide 300 mW pump power, 40 times threshold, and with 7-percent optical-conversion efficiency would give ~21 mW NdPP output. With this amount of pump power available, one would certainly choose to increase the output coupling for greater efficiency. From our measurements using collinear pumping, we anticipate that use of a 2- to 5-percent transmission output mirror would increase the transverse optical power-conversion efficiency to about 12 percent, yielding 36 mW output. With a value of 5 to 10 percent for the diode efficiency, an electrical input of 3 to 6 W to the diode array would be required. These figures are extrapolated from the single-diode configuration; using more than one pump array (i. e., one on either side of a thin NdPP crystal) might give more output power, but lower efficiency without a back-surface reflector. Also, excellent heat-sinking will probably be required to dissipate most of the heat generated in the diode array. The optical-power dissipation in the NdPP crystal should not be a limitation, since we have obtained 50-mW CW operation from a NdPP crystal collinearly pumped at 0.58 μm .

These parameters establish an approximate range of powers which should be practical in a miniature NdPP laser device. As Singh *et al.*⁷ have pointed out, Nd:YAG is a better laser material than NdPP in terms of its Nd^{3+} emission cross section and fluorescent lifetime. However, these properties can be utilized best in large laser rods which allow substantial absorption of pump radiation. For miniature lasers with low power requirements, concentrated rare-earth crystals such as NdPP offer the best potential for future development. In the process of miniaturization, further reduction in the overall laser-cavity size could be obtained using small graded-index rod (GRIN) reflectors⁸ to replace the present spherical mirrors.

Other materials such as $\text{LiNdP}_4\text{O}_{12}$ (see Refs. 9 and 10, and Sec. B below) have also exhibited low thresholds and have lased in the transverse configuration.¹¹ Depending on crystal size availability and laser power requirements, it also might be desirable to reduce the Nd concentration somewhat in crystals such as $\text{Nd}_x\text{La}_{1-x}\text{P}_5\text{O}_{14}$, as has been suggested in Ref. 7, in order to obtain somewhat longer fluorescent lifetimes, at the expense of decreased pump absorption.

S. R. Chinn
J. W. Pierce
H. Heckscher

B. LOW-THRESHOLD, CW $\text{LiNdP}_4\text{O}_{12}$ LASER

We have obtained low-threshold, room-temperature, CW laser action in $\text{LiNdP}_4\text{O}_{12}$ (LNP). (This compound has been called LiNd-ultraphosphate,⁹ but the nomenclature¹² appropriate to the $\text{LiNdO}_2/\text{P}_2\text{O}_5$ ratio is LiNd-metaphosphate.) Yamada, Otsuka, and Nakano⁹ have characterized the fluorescence properties of LNP and reported pulsed lasing. In our experiments, we have excited LNP with a CW dye laser and measured the laser threshold, output spectrum, and power-conversion efficiency.

As with $\text{NdP}_5\text{O}_{14}$ (NdPP) and its solid solutions,¹³⁻¹⁵ LNP includes Nd as a stoichiometric constituent rather than as a low-concentration dopant. Because neighboring Nd^{3+} ions are separated by O-P-O groups, the radiative decay from the $^4\text{F}_{3/2}$ state does not suffer severe concentration quenching;¹⁶ consequently, LNP is a material with long radiative lifetime ($\tau = 120 \mu\text{sec}$) and large emission cross section ($\sigma = 9 \times 10^{-19} \text{ cm}^2$) at high Nd^{3+} concentration ($N_0 = 4.37 \times 10^{21} \text{ cm}^{-3}$) (see Ref. 9). This high concentration results in very short absorption lengths for the higher-energy transitions in the Nd^{3+} excitation spectrum. These factors lead to extremely efficient excitation and very low laser thresholds for small LNP samples.

Our experimental procedure was similar to that described by previous workers,¹³⁻¹⁵ except that the LNP was pumped with a CW Rhodamine 6G dye laser excited by an argon-ion laser. The pump radiation at 0.58 μm was focused collinearly onto the laser sample in the center of a nearly spherical optical cavity with 5-cm-radius mirrors. The input mirror had high reflectivity ($R > 99.9$ percent) at 1.05 μm , and the output mirror had approximately 0.3-percent transmission at 1.05 μm . A Corning 2-64 glass filter transmitted the 1.05- μm lasing radiation, but not the 0.58- μm pump, to a calibrated Si photodiode or to a grating spectrometer followed by an S-1 photomultiplier. In many of the measurements the pump beam was interrupted by a tuning-fork chopper, the pulsed laser output was displayed on an oscilloscope, and the output spectrum was recorded using phase-sensitive detection. The input power was measured by another calibrated Si photodiode inserted in the cavity immediately before the sample.

Instead of growing LNP crystals by the Kyropoulos pulling technique,⁹ we have obtained our crystals by a flux method. The starting materials were reagent grade Li_2CO_3 , $\text{NH}_4\text{H}_2\text{PO}_4$, and Nd_2O_3 , with a large excess of Li_2CO_3 and $\text{NH}_4\text{H}_2\text{PO}_4$ used as a flux. In a typical run, 11 g of Li_2CO_3 , 86 g of $\text{NH}_4\text{H}_2\text{PO}_4$, and 20 g of Nd_2O_3 were mixed in a 50-cm³ Pt crucible and fired at 950°C until no further weight loss was observed. The temperature was then reduced at 2°/hour to 700°C, and the power was turned off.

X-ray diffraction analysis of our crystals showed that LNP is monoclinic, with space group $C2/c$, lattice constants $a = 16.408 \text{ \AA}$, $b = 7.035 \text{ \AA}$, $c = 9.729 \text{ \AA}$, and $\beta = 126.38^\circ$. Like NdPP (see Refs. 17 and 18), whose space group was at first incorrectly identified¹⁹ because its deviation from orthorhombic symmetry is small, LNP (with suitably relabeled axes) also has a nearly orthorhombic space group ($Imma$), its originally reported structure.⁹

Generally, the best crystals were quite small. Because the optical quality varied, we report results only from our best sample to date, an as-grown, diamond-shaped platelet with thickness $l = 158 \mu\text{m}$ and approximately $0.5 \times 0.5 \text{ mm}^2$ in cross section. Lasing was along the normal to the platelet, the $\langle 001 \rangle$ axis, with linearly polarized output approximately parallel to the real-space "a" direction.

For pump radiation at 0.582 μm , which was almost completely absorbed, the threshold power was 360 μW incident on the sample for both CW and chopped operation. Using a 150-Hz chopping frequency with a 20-percent duty cycle, we measured the output power as a function of input power (Fig. II-6). For 1-mW quasi-CW output, the total power-conversion efficiency was 18 percent. With chopped excitation, characteristic relaxation oscillations were observed, as shown in Fig. II-7(a-b). These oscillations were analyzed²⁰ to estimate the cavity losses and laser mode saturation parameter.

For CW operation, the output power was reduced because of thermal effects (the sample was cemented at only one corner, and thus had practically no contact with any heat sink). We measured CW output powers up to 0.21 mW (with 2.35 mW input), but did not attempt to obtain higher levels.

It is interesting to estimate the value of η , the differential power efficiency expected for a given η_i (the internal differential quantum efficiency). The external differential quantum efficiency is given by²¹

$$\eta = \eta_i / [1 + 2\alpha l / \ln(1/R_1 R_2)]$$

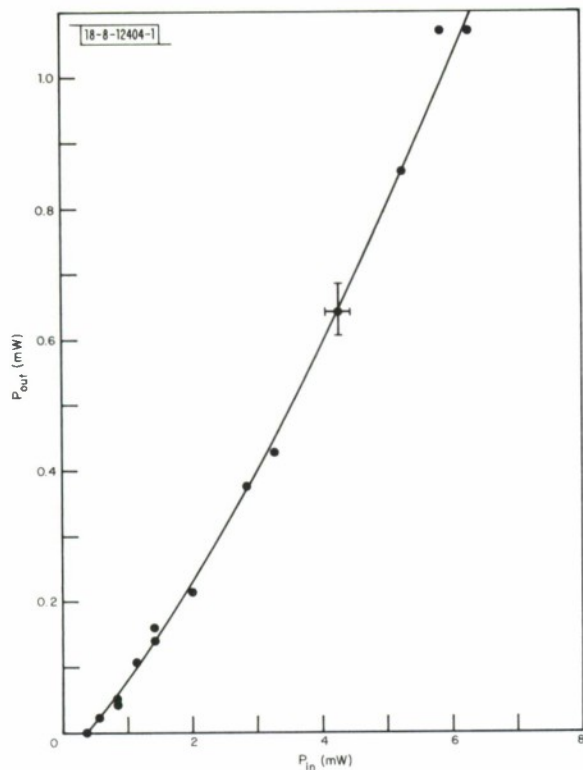
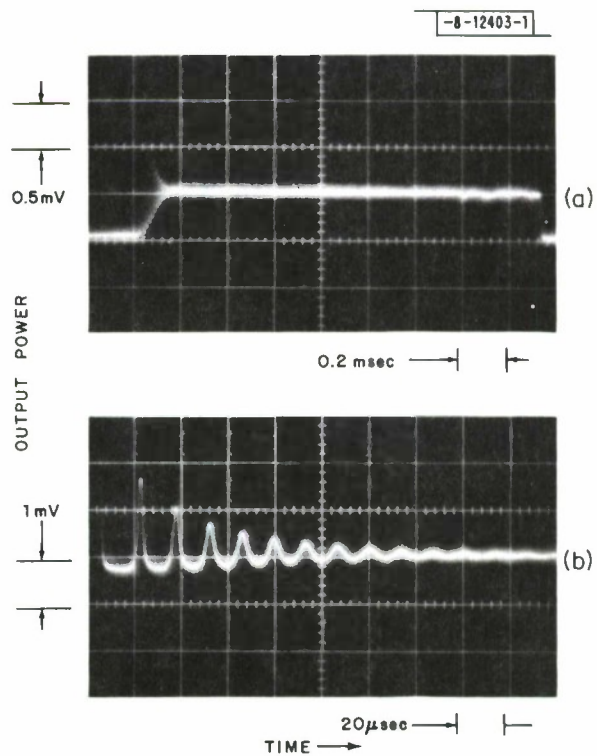


Fig. II-6. $\text{LiNdP}_4\text{O}_{12}$ laser output power P_{out} at $1.048\text{-}\mu\text{m}$ wavelength as function of input power P_{in} at $0.582\text{-}\mu\text{m}$ wavelength with 150-Hz , 20-percent duty-cycle chopped excitation. Sample thickness was $l = 158\text{ }\mu\text{m}$.

Fig. II-7. Laser relaxation oscillations in $\text{LiNdP}_4\text{O}_{12}$; in both (a) and (b), power calibration factor is 0.107 mW/mV .



where l = sample length, and R_1 and R_2 are the mirror reflectivities. For the loss term $2\alpha l$, we use an approximate value 3×10^{-3} found by analysis of the relaxation oscillations. With $\ln(1/R_1 R_2) \approx 3 \times 10^{-3}$ and a photon energy ratio of $0.582/1.05 \mu\text{m} = 0.56$, we obtain $\eta \approx 0.28 \eta_i$. If $\eta_i = 100$ percent, then $\eta \sim 28$ percent, compared with the 20-percent value obtained from the data in Fig. 11-6.

A note of caution should be given concerning the quantitative analysis of the relaxation oscillations, since Danielmeyer²² has shown that the results of Ref. 20 are not exact for the present situation of nonuniform (i. e., Gaussian) excitation of the Gaussian laser mode. Nevertheless, the simple analysis gives plausible results. For example, for input power levels of 16.4 and 3 times threshold (in ratio 5.5:1), the relaxation oscillations yield values of the saturation parameter (the ratio of spontaneous to stimulated lifetimes) equal to 33.6 and 5.96, respectively. The ratio of these values is 5.6:1, close to the pumping ratio as expected.

To estimate the gain at threshold, we use the expression

$$\sigma(N_u - N_l) l \approx \frac{2P_o \sigma \tau b}{h\nu_p \pi(w_o^2 + w_p^2)} - \sigma l N_o e^{-\Delta E/kT}$$

where N_u and N_l are the populations of the upper and lower laser levels, P_o is the threshold power, $\Delta E \approx 1950 \text{ cm}^{-1}$ is the separation of the levels,⁹ $b = 0.80$ in the Boltzmann population factor for the lower $^4F_{3/2}$ level, and w_o and w_p are the pump and laser mode radii. The pump waist w_p was measured to be $\sim 10 \mu\text{m}$, and we estimate that $w_o \approx 20 \mu\text{m}$. With these parameters, one finds $(N_u - N_l) \approx 0.43 \times 10^{18} \text{ cm}^{-3}$ and $2\sigma(N_u - N_l)l = 0.012$, giving the gain $G = \exp[2\sigma(N_u - N_l)l] = 1.012$. If we use a value for $2\alpha l = 8 \times 10^{-3}$, consistent with the measured power efficiency, then the total cavity loss is 0.011, somewhat similar than the estimated excess gain 0.012. This value for the total loss is roughly twice that found from the relaxation oscillations. The higher value of inversion and lower value of efficiency than expected may result from worse-than-estimated matching of the pump and laser mode beam waists. Also, scattering losses at the sample surfaces would account for a higher threshold and lower external efficiency. Note, however, that reflective losses from the sample should not be significant if the sample is well aligned and acts as a wavelength-selecting etalon. In fact, the sum of the two surface reflectivities is about 10 percent, much higher than any of the loss estimates above, which tends to confirm the etalon effect of the sample.

The laser spectrum of LNP excited ten times above threshold is shown in Fig. 11-8. The longitudinal mode separation calculated for the sample acting as an etalon is

$$\Delta\lambda = \lambda^2/2nl = 22 \text{ \AA}$$

where the index of refraction $n = 1.58$ (see Ref. 9). No such spectral spacing is seen; the small line adjacent to the dominant one is probably a higher-order transverse mode. The absence of other longitudinal modes may come from linewidth limitations [full-width, half-maximum $\sim 20 \text{ \AA}$ (see Ref. 9)], although at ten times above threshold one would expect to see more than one such mode.

S. R. Chinn
H. Y.-T. Hong

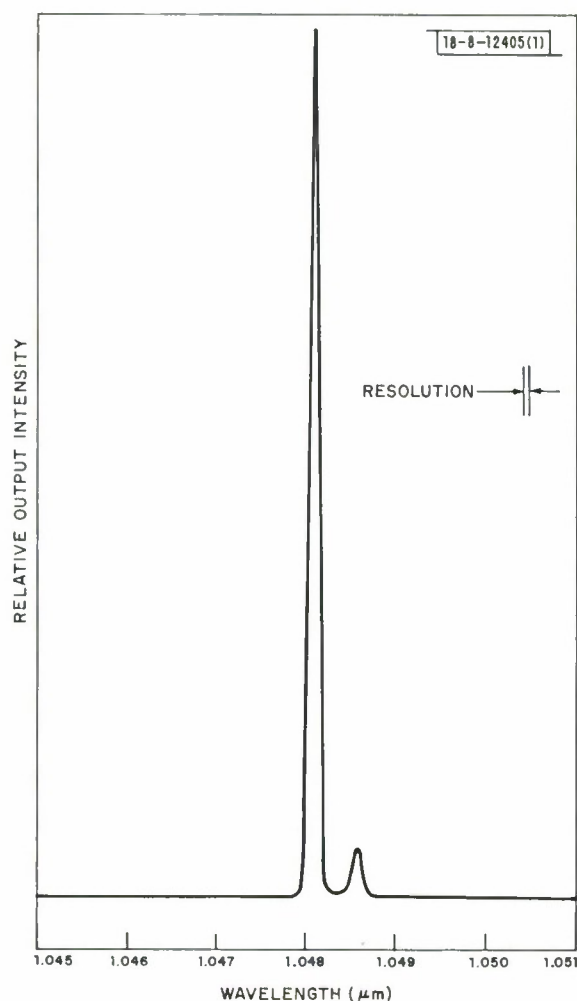


Fig. II-8. Lasing output spectrum of LiNdP₄O₁₂ excited ten times above threshold with 150-Hz, 20-percent duty-cycle, chopped excitation.

C. EXTERNAL-CAVITY CO₂-PUMPED InSb SPIN-FLIP LASER

The use of an external-cavity spin-flip Raman laser is described here in which the axial and transverse modes can be carefully controlled to provide a device that is potentially useful for spectroscopic and photochemical applications. In the past, spin-flip lasers in the usual form of a rectangular parallelepiped produced a spectrally poor output when operated at high drive levels.^{23,24} This is particularly true for high carrier-concentration InSb crystals ($n \sim 1 \times 10^{16} \text{ cm}^{-3}$) in high magnetic fields that are needed for high-energy pulsed operation in the 11- to 13- μm region because the spontaneous spin-flip linewidth²⁵ ($\sim 0.2 \text{ cm}^{-1}$) is comparable to the Fabry-Perot cavity linewidths. The spin-flip output then has limited tuning within a mode, with large jumps between modes. This is in contrast to the situation in low-concentration samples at low magnetic fields (1 to 10 kG) where the spontaneous linewidths²⁶ are only a few hundred megahertz. In addition, internal bounce-mode operation can degrade the spectral characteristics as well as substantially limit the external conversion efficiency. In order to improve this situation, we have operated the spin-flip laser in an external-cavity geometry where bounce modes are eliminated and the cavity-mode frequencies can be altered independently of the magnetic field to allow complete control of the spin-flip laser output frequency. In addition, the use of resonant

output couplers results in a narrowed spin-flip spectral output. At present, with a low-finesse uncoated Ge output coupler, we have obtained a spin-flip output spectral width $<0.027 \text{ cm}^{-1}$.

The cavity geometry used here consisted of an InSb crystal ($n \sim 4.2 \times 10^{16} \text{ cm}^{-3}$) antireflection-coated on both ends mounted on a cold finger ($T \sim 20 \text{ K}$) in the bore of a split superconducting solenoid. Sample dimensions are $0.75 \times 0.75 \text{ cm}$ cross section by 1.5 cm long. A 1-m -radius gold mirror could be mounted on the dewar output window flange with a bellows arrangement that allows its alignment to be adjusted under vacuum. An NaCl Brewster angle window was mounted in the opposite window flange, and an output coupler completed the optical cavity. Both ZnSe and Ge (uncoated) output couplers were used. The overall cavity length was 30 cm . Pump laser radiation was introduced through the output coupler, while the spin-flip output was separated out using a dichroic beamsplitter and a spectrometer. In order to provide a spectrally narrow pump source, a CW gain cell was operated in the CO_2 TEA laser cavity to force the laser to operate in a single longitudinal mode. Apertures constrained the output to a TEM_{00} mode. The CO_2 beam was collimated to a spot size of approximately 2-mm diameter which matches the $12\text{-}\mu\text{m}$ spot size for the spin-flip cavity parameters.

The uncoated output coupler acts as a resonant reflector because of its Fabry-Perot modes, and serves a dual role as output coupler and frequency-selective etalon. The set of coupled Fabry-Perot cavities together with their free spectral ranges (fsr) involved in the observed tuning characteristics are the overall cavity 30 cm ($\text{fsr} = 0.017 \text{ cm}^{-1}$) and one of the following three output couplers: (1) Ge etalon 2.23 mm ($\text{fsr} = 0.56 \text{ cm}^{-1}$), (2) Ge etalon 3.2 mm ($\text{fsr} = 0.39 \text{ cm}^{-1}$), and (3) Ge etalon 9.6 mm ($\text{fsr} = 0.13 \text{ cm}^{-1}$).

The spin-flip laser mode-tuning characteristics at an output wavelength of $12.2 \mu\text{m}$ were measured with a 1-cm^{-1} fsr Fabry-Perot interferometer and are shown in Fig. II-9(a) for the case of a 3.2-mm -thick Ge output coupler. The output spectrum is dominated by the Fabry-Perot modes of the output coupler; the overall cavity Fabry-Perot modes are too finely spaced to be observable. The spacing of $0.38 \pm 0.04 \text{ cm}^{-1}$ is in good agreement with the calculated etalon spacing of 0.39 cm^{-1} . The tuning rate within a mode is 9.3 MHz/G , and the tuning range of a single mode is about 0.13 cm^{-1} . More complex spectra were observed with the 2.23-mm Ge output coupler because of broader etalon modes. A plot of the dominant output line of the spin-flip laser with magnetic field for the 2.23-mm etalon is shown in Fig. II-9(b). The mode spacing of $0.63 \pm 0.06 \text{ cm}^{-1}$ is in agreement with the calculated etalon spacing.

With a 9.6-mm -thick output coupler, the spin-flip output frequency was determined solely by the Fabry-Perot modes of the output coupler to within the 0.05-cm^{-1} resolution of the measurement. Varying the magnetic field resulted in the spin-flip laser output frequency jumping from one etalon mode to the next. The narrowest spectral output was obtained with this output coupler. Figure II-10 shows a Fabry-Perot trace of the output spectrum taken with a 0.13-cm^{-1} free spectral range Fabry-Perot. The top trace shows the CO_2 pump laser spectral output, and the bottom trace is the spin-flip laser output. The measured spectral width is $0.027 \pm 0.003 \text{ cm}^{-1}$, after allowing for the Fabry-Perot resolution. The modes of the overall cavity, of which there were probably no more than two, could not be resolved in this trace. Single-frequency operation should be possible with higher finesse output couplers.

The control of the spin-flip laser output frequency by the resonant output coupler provides a convenient means of fine-tuning this frequency. A tunable output coupler could be constructed from two Ge windows, AR-coated on one side, separated by a piezoelectric cylinder which can

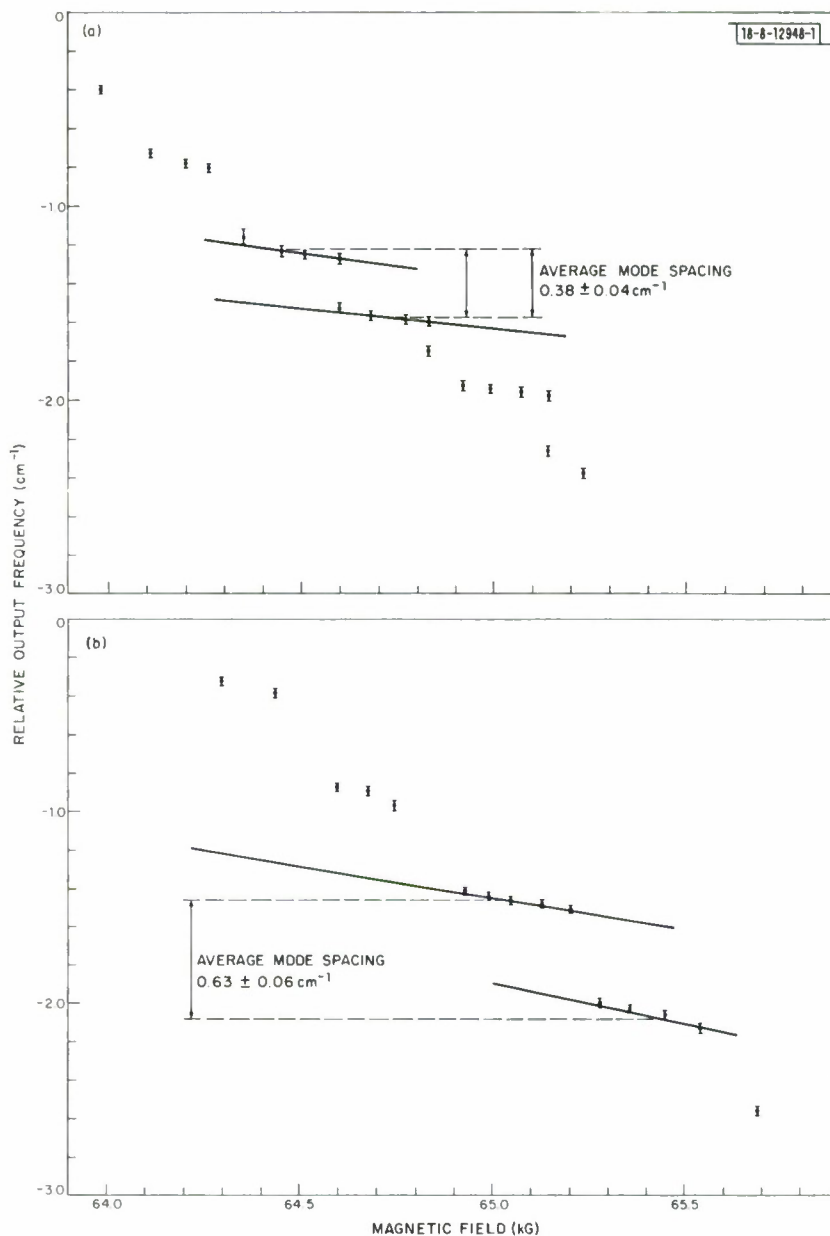


Fig. II-9. Tuning characteristics of external-cavity spin-flip laser with (a) 3.2-mm and (b) 2.3-mm-thick Ge output couplers.

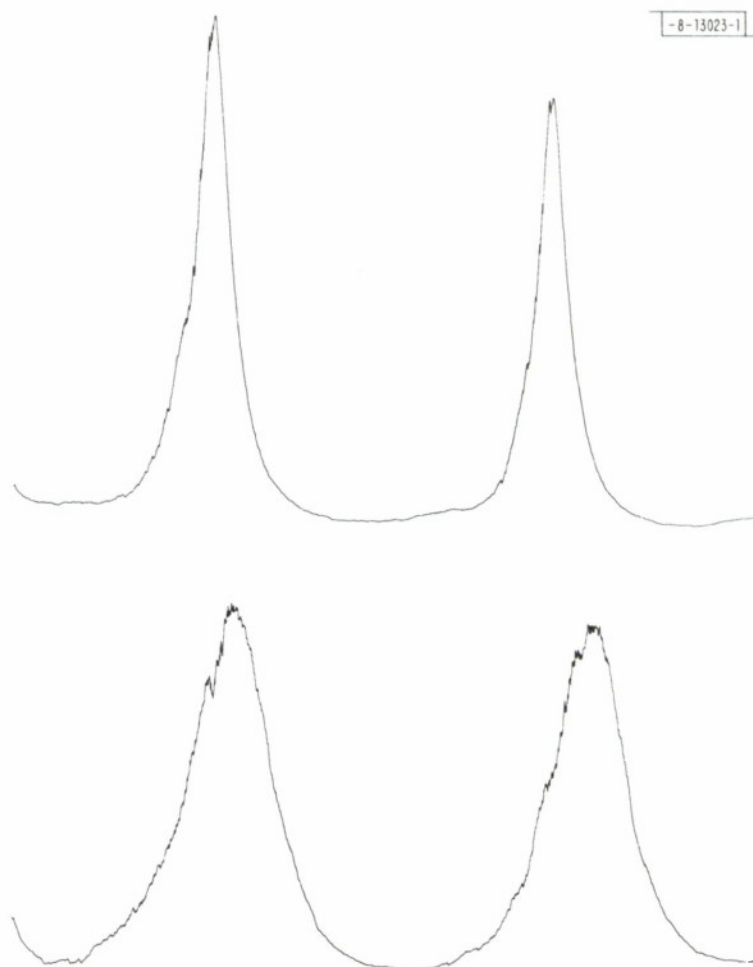


Fig. II-10. Fabry-Perot spectral traces, 0.13 cm^{-1} free spectral range: (top) CO_2 pump laser, and (bottom) $12\text{-}\mu\text{m}$ spin-flip laser output ($H = 58 \text{ kG}$, $T \sim 20 \text{ K}$, $n = 1.2 \times 10^{16} \text{ cm}^{-3}$).

be voltage-tuned over a free spectral range. Alternatively, the temperature dependence of the Ge index of refraction²⁷ [$(1/n) (dn/dT) = 6.9 \pm 0.4 \times 10^{-5}/K$] could be exploited to temperature-tune the output coupler. For a 1-cm-thick Ge etalon, a temperature variation of only 2 K is required to tune over a free spectral range. By sweeping the magnetic field in synchronism with the temperature, continuous tuning over a relatively broad range should be readily attainable.

The spin-flip output-pulse shape does not simply follow the time dependence of the pump laser, but rather shows only a short (~ 50 nsec) output pulse even when long input pulses of about 1- μ sec duration are used. This behavior is due to a combination of transient behavior of the saturable Raman medium and gain reduction due to free carrier absorption. These effects will be discussed in more detail in a future report. The spectral data presented above were obtained at maximum output energy levels of about 50 to 60 μ J.

In summary, the CO_2 -pumped spin-flip laser has been operated in an external-cavity geometry in which the output frequency of the spin-flip laser is governed to a large extent by the Fabry-Perot modes of a resonant output coupler. By tuning this output coupler in tandem with the magnetic field, essentially complete frequency coverage with single-mode operation can be obtained and should enhance the usefulness of the spin-flip laser for many applications.

S. R. J. Brueck
A. Mooradian

D. OPTICALLY PUMPED C_2H_2 , CS_2 , AND SiH_4 LASERS

Optically pumped laser systems for generating new infrared frequencies are being studied. Such infrared sources have potential application in laser-induced isotope separation and photochemistry. In a previous Solid State Research Report,²⁸ OCS laser action in the 8.2- to 8.4- μ m region was reported; optically pumped CO_2 and N_2O laser action also was reported. Here, we report optically pumped laser action in three other molecules: C_2H_2 , CS_2 , and SiH_4 . This is the first report of laser action in silane, SiH_4 .

These lasers are transfer lasers based on optical excitation of CO gas by a frequency-doubled, single-line CO_2 TEA laser. The vibrationally excited CO molecules transfer energy into a second gas where laser action occurs. The technique now has been demonstrated for mixtures of CO with OCS, CO_2 , N_2O , C_2H_2 , CS_2 , and SiH_4 . Only one other optical transfer laser has been reported previously: an HBr TEA laser was used to pump CO_2 with subsequent energy transfer into N_2O (see Ref. 29).

The CO molecule is ideal for storage of vibrational energy because of its exceedingly slow vibration to translation transfer rate of $1.9 \times 10^{-3} \text{ sec}^{-1} \text{ Torr}^{-1}$ (see Ref. 30). The second harmonic of the P(24) line of the 9.6- μ m CO_2 band falls within 0.003 cm^{-1} of the CO $0 \rightarrow 1$ P(14) transition and is efficiently absorbed. Nearly resonant energy transfer from the CO molecule makes it possible to vibrationally excite a number of molecules without requiring an exact frequency match between the pump laser and the active molecule, as is the case for direct optical excitation; with CO_2 , for example, the mismatch is 206 cm^{-1} .

Optical transfer pumping is a useful technique for investigating potential laser systems, and allows the determination of important laser parameters in a well-defined system. The excitation energy is usually deposited into a specific vibrational mode, and the dissociation problems which often are encountered with conventional electronic discharge excitation are avoided.

The experimental configuration has been shown previously.²⁸ The output of a grating-controlled Lumonics TEA laser is passed through a telescope which reduces the beam diameter

to about 4 mm. The energy incident upon the uncoated CdGeAs_2 (Ref. 31) doubling crystal is typically 300 mJ and is contained in a 200-nsec pulse (FWHM). The doubling crystal, with a cross section of $7 \times 13 \text{ mm}^2$ and a length of 12 mm, has produced up to 26 mJ of second-harmonic energy at an external energy-conversion efficiency of 8 percent without damage. The crystal was cooled to 77 K to minimize absorption. Laser cavities with internal mirrors and lengths ranging from 0.4 to 30 cm were used. The dielectric-coated Ge input mirrors had a 1-m radius, a transmission in excess of 50 percent at $4.8 \mu\text{m}$, and a reflectivity of 99 percent at the laser wavelength. The back mirror was a broadband 100-percent reflector with a radius of 30 cm. The input energy to the cell and the output energy were measured using calibrated pyroelectric detectors. The output wavelengths were measured using a 1-m grating spectrometer.

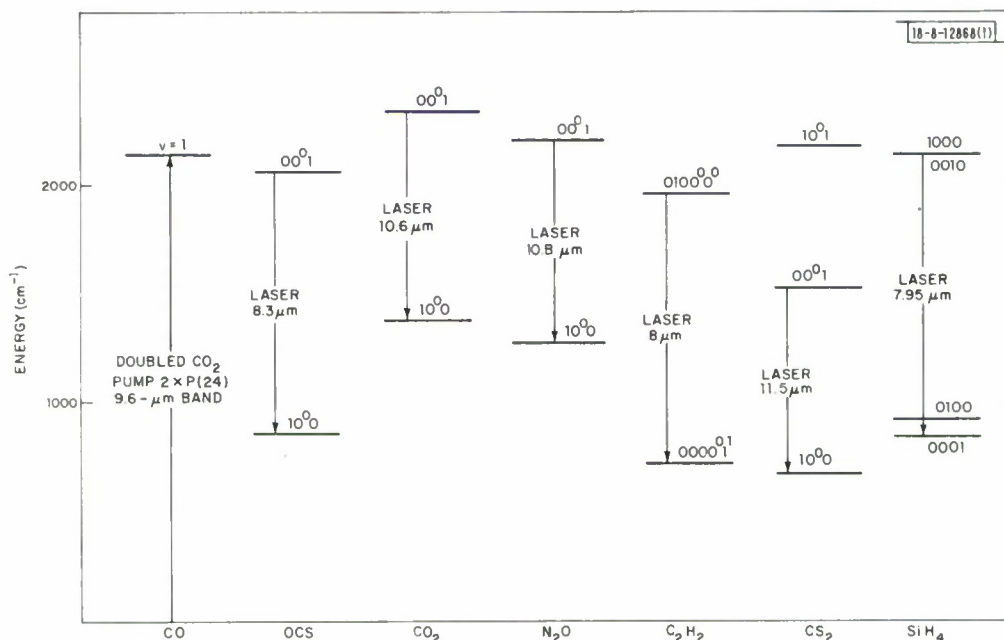


Fig. II-11. Simplified energy-level diagram for CO and molecules pumped by nearly resonant energy transfer.

Figure II-11 shows a simplified energy-level diagram for the CO and the lasing molecules, while Table II-1 summarizes the measurements. Not all quantities in the table were obtained under the same conditions; for example, maximum output energy is generally not obtained at maximum pressure. The quoted efficiencies are slope efficiencies obtained from plots of output vs.-input energy to the gas. The CO absorbed most of the input energy at the pressures of interest.

The $\text{CO-C}_2\text{H}_2$ laser uses the near resonance between the CO ($v = 1$) level at 2143 cm^{-1} and the C_2H_2 0100^0_0 level at 1974 cm^{-1} (Ref. 32) for transfer pumping. In contrast to the other molecules reported on here, the transfer is to a vibrational mode having no dipole moment. Laser action in acetylene was reported first by Shelton and Byrne.³³ They excited $\text{C}_2\text{H}_2\text{-H}_2\text{-He}$ mixes in a pulsed electrical discharge and observed an output near $8 \mu\text{m}$, which they attributed

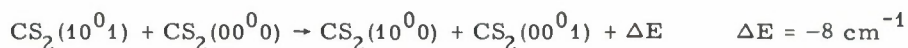
TABLE II-1					
SUMMARY OF PERFORMANCE OF OPTICALLY PUMPED LASERS					
System	Maximum Pressure (Torr)	Minimum Threshold		Maximum Efficiency (percent)	Maximum Output (mJ)
		Focused (mJ)	Unfocused (mJ)		
OCS (direct-pumped)	55	0.1	0.6	4.0	0.25
CO-OCS	115	0.1	1.0	2.0	0.15
CO-CO ₂	760*	—	1.6	7.3	0.48
CO-N ₂ O	760*	—	2.0	5.6	0.35
CO-C ₂ H ₂	36	—	4.0	0.5	0.025
CO-C ₂ H ₂ -H ₂	140	—	4.0	1.5	0.09
CO-CS ₂	—	—	2.5	0.1	0.01
CO-CS ₂ -H ₂	20	—	5.0	0.5	0.03
CO-SiH ₄	35	2.2	—	0.6	0.03
*Limit of gas-handling system.					

TABLE II-2	
OBSERVED VACUUM FREQUENCIES OF THE C ₂ H ₂ LASER	
This Work (cm ⁻¹)	Previous Measurements* (cm ⁻¹)
—	1244.70
1244.52	1244.46
1244.12	1244.09
1243.75	1243.64
1243.08	1243.12
*C. F. Shelton and F. T. Byrne, Appl. Phys. Lett. <u>17</u> , 436 (1970).	

to Q-branch transitions of the $0100^0_0 \rightarrow 000^0_1$ band. Table II-2 lists our observed frequencies, along with their measurements. The 0.09-mJ output of the optically pumped laser is greater than the 0.06 mJ obtained previously with 1 J of electrical input to a larger laser.

Although it was not necessary for obtaining laser action, the addition of hydrogen to give a 1:1:1 CO-C₂H₂-H₂ mix increased the maximum operating pressure, the output energy, the slope efficiency, and the output pulse width of the acetylene laser. However, the addition of hydrogen did not change the threshold for laser action. These facts indicate that in our system the role of hydrogen is to depopulate the lower laser level.

Laser action in CO-CS₂ mixes occurred near 11.5 μ m. The CS₂ laser was first demonstrated by Patel using N₂-CS₂ mixes and DC electrical excitation.³⁴ More recently, pulsed laser action on some of the lines seen by Patel was obtained using an e-beam system to excite CO-CS₂-H₂ mixes.³⁵ Several different assignments for the observed lines have been proposed, including the $00^0_1 \rightarrow 10^0_0$ and $02^0_1 \rightarrow 12^0_0$ transitions.^{36,37} For our laser, the CO-CS₂ transfer is most likely to occur to the 10^0_1 combination band, which lies 42 cm⁻¹ above the CO ($v = 1$) level. The measured transfer rate, 1.4×10^4 Torr⁻¹ sec⁻¹, is orders of magnitude too large to be accounted for by direct transfer to the fundamental, which lies 608 cm⁻¹ away.^{38,39} The 01^1_1 and 02^0_1 levels which have been suggested as upper laser levels are both farther from resonance than the 10^0_1 level, and they therefore are probably not important. However, the 10^0_1 combination band can break up into two fundamental modes by the nearly resonant process,



which should occur in a few collisions. This leads to population in both the upper and lower laser levels so that differential relaxation is needed to produce an inversion. This may account for the relatively poor efficiency of the optically pumped CS₂ system. Breakup into fundamental vibrations also can occur if other combination bands are pumped, and this was probably the case for Patel's N₂-CS₂ laser, where the 02^0_1 level was in near resonance with the vibrationally excited nitrogen. These energy transfer considerations suggest that lasing will occur on the $00^0_1 \rightarrow 10^0_0$ transitions, and this assignment is supported by our wavelengths measurements.

The wavelengths of the CS₂ laser were measured using a 1-m grating spectrometer. A total of 11 lines was measured with an absolute accuracy of better than 0.04 cm⁻¹. Table II-3 lists the observed frequencies together with the measurements by Patel and the calculated frequencies for the three possible transitions $00^0_1 \rightarrow 10^0_0$, $01^1_1 \rightarrow 11^1_0$, and $10^0_1 \rightarrow 20^0_0$. It is clear from the table that the measurements are only consistent with lasing on the $00^0_1 \rightarrow 10^0_0$ transition. We therefore conclude that for the optically pumped CO-CS₂-H₂ laser, the transfer is into a combination band, while the lasing occurs from a fundamental vibration.

As in the case of C₂H₂, the addition of hydrogen increased the output energy and the pulse length of the CS₂ laser, and the effect is attributed to depopulation of the lower laser level.

The molecules discussed above are all linear molecules consisting of 3 or 4 atoms. Obtaining laser action for larger nonlinear molecules is expected to be generally more difficult, since the number of modes of vibration and thus the number of energy levels will increase. The greater number of levels increases the number of channels for vibrational relaxation, and makes the production of an inversion more difficult. The relaxation problem can be overcome by using direct rather than transfer pumping, and operating at sub-Torr pressures where no collisions occur during the pump pulse. This approach has been used to produce optically pumped laser action in SF₆ (see Ref. 40).

TABLE II-3						
OBSERVED CS ₂ LASER LINES AND CALCULATED FREQUENCIES FOR POSSIBLE LASER TRANSITIONS (in vacuum cm ⁻¹)						
Observed Laser Lines		Calculated Transition Frequencies (±0.02 cm ⁻¹)				
This Work (±0.04 cm ⁻¹)	Patel* (±0.02 cm ⁻¹)	00 ⁰ ₁ → 10 ⁰ ₀ [†]		01 ¹ ₁ → 11 ¹ ₀ [†]		10 ⁰ ₁ → 20 ⁰ ₀ [‡]
871.37	—	P(26)	871.33	P(30)	871.35	P(2) 871.33
870.78	870.90	P(28)	870.82	P(32)	870.84	P(4) 870.89
870.33	870.38	P(30)	870.32	P(34)	870.33	P(6) 870.45
—	869.85	P(32)	869.82	P(36)	869.81	P(8) 870.00
869.35	869.33	P(34)	869.31	P(38)	869.28	P(10) 869.54
—	868.82	P(36)	868.80	P(40)	868.76	P(14) 868.62
868.32	868.31	P(38)	868.28	P(42)	868.22	P(16) 868.15
—	867.80	P(40)	867.77	P(44)	867.68	P(18) 867.68
867.29	867.27	P(42)	867.23	P(46)	867.14	P(20) 867.20
—	866.73	P(44)	866.72	P(48)	866.60	P(22) 866.72
866.17	866.20	P(46)	866.17	P(50)	866.04	P(24) 866.24
865.57	—	P(48)	865.63	P(52)	865.48	P(26) 865.75
865.08	—	P(50)	865.09	P(54)	864.92	P(28) 865.25
864.46	—	P(52)	864.54	P(56)	864.36	P(30) 864.75
863.38	—	P(56)	863.43	P(60)	863.21	P(36) 863.23
*C. K. N. Patel, Appl. Phys. Lett. <u>7</u> , 273 (1965). †D. F. Smith, Jr., T. Chaa, J. Lin, and J. Overend, Spectrochim. Acta <u>27A</u> , 1979 (1971). ‡A. G. Maki and R. L. Sams, J. Mol. Spectrosc. <u>52</u> , 233 (1974).						

We have been able to obtain laser action at $7.95\text{ }\mu\text{m}$ in the CO-SiH_4 system at pressures up to 35 Torr. The observed vacuum frequencies are 1265.50, 1262.31, 1258.02, 1257.10, 1254.86, and 1251.25 cm^{-1} . This is the first report of laser action in silane and the first optically pumped laser action in a nonlinear molecule at pressures where both vibrational and rotational relaxation occur before lasing.

The multi-line spectrum obtained here is evidence of the rotational cross-relaxation; it should be possible to obtain laser action on even more lines by inserting a grating in the cavity. Transfer from CO can occur to either the 1000 level at 2185.7 cm^{-1} or the 0010 level at 2189.08 cm^{-1} . Laser action occurs from one or both of these levels to the 0001 level at 914 cm^{-1} .

The CO-SiH_4 ratio was optimum at 1:1, although ratios from 1:3 to 4:1 were operated. In contrast to C_2H_2 and CS_2 , the addition of hydrogen did not increase the output energy. Addition of helium also was tried, but this did not increase either the output energy or the operating pressure. In contrast, the addition of helium to CO-OCS and $\text{CO-C}_2\text{H}_2$ mixtures increased the operating pressures to 390 and 300 Torr, respectively, although it did not increase the output energy. The other measured parameters for the SiH_4 laser are listed in Table II-1.

T. F. Deutsch
H. Kildal

E. PULSED HETERODYNE MEASUREMENTS OF SUBMILLIMETER LASERS

In order to study the application of high-power, optically pumped lasers to a number of physical phenomena, we have extended our work on the CW submillimeter heterodyne receiver⁴¹ to the detection of short pulses. The system consists of a low-capacitance, small-junction-area, Schottky diode in which the pulsed-laser signal is mixed with a 74-MHz CW klystron. The beat frequency between the 8th harmonic of the klystron and the laser is fed into a 30-MHz IF strip and is video-detected.

In our initial testing of the heterodyne system, we examined the bandwidth of a pulsed CH_3F laser pumped by a CO_2 TEA laser and emitting at $496\text{ }\mu\text{m}$. The CO_2 laser pulse width was about 100 nsec, and the submillimeter output pulse was about 500-nsec long delayed by about 1 μsec . There is considerable fine structure in the methyl fluoride pulse. By means of simple cavity-tuning, the output frequency could be varied over 500 MHz. At a given resonator setting, the linewidth was less than 5 MHz, and the lasing peak could be located readily to a precision of better than 1 MHz.

C. D. Parker
H. R. Fetterman
P. E. Tannenwald

REFERENCES

1. Solid State Research Report, Lincoln Laboratory, M.I.T. (1975:1), p.17, DDC AD-A009848/3; S.R. Chinn, J.W. Pierce, and H. Heckscher, IEEE J. Quantum Electron. (to be published).
2. J. Stone and C.A. Burrus, Appl. Phys. Lett. 23, 388 (1973).
3. C.A. Burrus and J. Stone, Appl. Phys. Lett. 26, 318 (1975).
4. R.B. Chelser and D.A. Draegert, Appl. Phys. Lett. 23, 235 (1973); D.A. Draegert, IEEE J. Quantum Electron. QE-9, 1146 (1973).
5. M. Ettenberg, K.C. Hudson, and H.F. Lockwood, IEEE J. Quantum Electron. QE-9, 987 (1973).
6. J.M. Hammer, H. Kressel, I. Ladany, C.C. Niel, and W. Phillips, Proc. IEEE 63, 325 (1975); I. Ladany and H. Kressel, Appl. Phys. Lett. 25, 708 (1974).
7. S. Singh, D.C. Miller, J.R. Potopowicz, and L.K. Shick, J. Appl. Phys. 46, 1191 (1975).
8. J.C. Vanderleeden, J. Appl. Phys. 45, 201 (1974).
9. T. Yamada, K. Otsuka, and J. Nakano, J. Appl. Phys. 45, 5096 (1974).
10. S.R. Chinn and H. Y-P. Hong, Appl. Phys. Lett. 26, 649 (1975).
11. K. Otsuka and T. Yamada, Appl. Phys. Lett. 26, 311 (1975).
12. J.R. Van Wazer, Phosphorous and Its Compounds (Interscience, New York, 1958), Vol. 2, p.423.
13. H.P. Weber, T.C. Damen, H.G. Danielmeyer, and B.C. Tofield, Appl. Phys. Lett. 22, 534 (1973).
14. T.C. Damen, H.P. Weber, and B.C. Tofield, Appl. Phys. Lett. 23, 519 (1973).
15. H.G. Danielmeyer, G. Huber, W.W. Krühler, and J.P. Jeser, Appl. Phys. Lett. 2, 335 (1973).
16. H. Y-P. Hong and K. Dwight, Mater. Res. Bull. 9, 775 (1974), DDC AD-786294/9.
17. H. Y-P. Hong, Acta Crystallogr. B30, 468 (1974), DDC AD-A000491/1.
18. K.R. Albrand, T.R. Attig, J. Fenner, J.P. Jeser, and D. Mootz, Mater. Res. Bull. 9, 129 (1974).
19. H.G. Danielmeyer and H.P. Weber, IEEE J. Quantum Electron. QE-8, 805 (1972).
20. H.G. Danielmeyer, J. Appl. Phys. 41, 4014 (1970).
21. J.R. Biard, W.N. Carr, and B.S. Reed, Trans. AIME 230, 286 (1964).
22. H.G. Danielmeyer, private communication.
23. C.K.N. Patel and E.D. Shaw, Phys. Rev. Lett. 24, 451 (1970).
24. J.T. Ganley, F.B. Harrison, and W.T. Leland, J. Appl. Phys. 45, 4980 (1974).
25. S.R.J. Brueck, A. Mooradian, and F.A. Blum, Phys. Rev. B 7, 5253 (1973), DDC AD-772151/7.
26. S.R.J. Brueck and A. Mooradian, Opt. Commun. 8, 263 (1973), DDC AD-772118/6.
27. S.R.J. Brueck and A. Mooradian, IEEE J. Quantum Electron. (to be published).
28. Solid State Research Report, Lincoln Laboratory, M.I.T. (1974:4), p.33, DDC AD-A004763/9.
29. T.Y. Chang and O.R. Wood, Appl. Phys. Lett. 24, 182 (1974).
30. M.A. Kovacs and M.E. Mack, Appl. Phys. Lett. 20, 487 (1972).

31. H. Kildal and J. C. Mikkelsen, Opt. Commun. 10, 306 (1974), DDC AD-A000516/5.
32. E. E. Bell and H. H. Nielsen, J. Chem. Phys. 18, 1382 (1950).
33. C. F. Shelton and F. T. Byrne, Appl. Phys. Lett. 17, 436 (1970).
34. C. K. N. Patel, Appl. Phys. Lett. 7, 273 (1965).
35. L. Y. Nelson, C. H. Fisher, and S. R. Byron, Appl. Phys. Lett. 25, 517 (1974).
36. A. G. Maki, Appl. Phys. Lett. 11, 204 (1967).
37. N. Legay-Sommaire, Appl. Phys. Lett. 12, 34 (1968).
38. D. C. Richman and R. C. Millikan, J. Chem. Phys. 61, 4263 (1974).
39. J. K. Hancock, D. F. Starr, and W. H. Green, J. Chem. Phys. 61, 3017 (1974).
40. H. R. Fetterman, H. R. Schlossberg, and W. E. Barch, 1975 Conference on Laser Engineering and Applications, Washington, D.C., May 1975.
41. H. R. Fetterman, B. J. Clifton, P. E. Tannenwald, C. D. Parker, and H. Penfield, IEEE Trans. Microwave Theory Tech. MTT-22, 1013 (1974), DDC AD-A011324/1.

III. MATERIALS RESEARCH

A. PHOTOELECTROLYSIS OF WATER

Photoelectrolysis, a process in which a semiconductor is used to catalyze the decomposition of water by light,¹ is potentially an important method for the utilization of solar energy to produce gaseous H_2 , a fuel that is conveniently transported and stored. We have been investigating the physics and electrochemistry of photoelectrolysis by experiments in which an n-type semiconducting anode (either TiO_2 or $SrTiO_3$) and a platinized-Pt cathode are immersed in an aqueous electrolyte and connected externally to form a photochemical cell.^{2,3} When the anode is illuminated, electron-hole pairs are generated at its surface by absorption of photons with energies exceeding its bandgap (3.0 eV for TiO_2 , 3.2 eV for $SrTiO_3$). If the energy bands of the anode are bent at its interface with the electrolyte, the photon-generated carriers are separated: the electrons move into the bulk of the anode and then through the external circuit to the cathode where they can interact with the water of the electrolyte solution to produce H_2 , while the holes remain at the surface of the anode where they interact with water to produce O_2 . Thus, the decomposition of water can be accomplished by the action of photons with energies far below the threshold for direct photodecomposition, which is about 6.5 eV.

In experiments reported earlier,³ we measured the short-circuit current and the amount of oxygen evolved for cells with single-crystal or polycrystalline TiO_2 anodes, as a function of the wavelength of monochromatic light used for illumination. For photon energies close to 4 eV, values as high as 80 to 85 percent were obtained for the external quantum efficiency η , defined as the ratio of the number of electrons flowing in the external circuit to the number of photons incident on the cell. Taking account of losses due to reflection at the interfaces and absorption in the electrolyte, we found that the maximum internal quantum efficiency of O_2 evolution was close to 100 percent. On the assumption that H_2 was being generated at the cathode, we concluded that the efficiency of photoelectrolysis with TiO_2 anodes was also close to 100 percent.

In the experiments described, however, the electrochemical cells were open to the air so that there was a plentiful supply of dissolved oxygen in the electrolyte surrounding the cathode. We subsequently have found that under these conditions H_2 is not generated, although one O_2 molecule is generated at the anode for every four electrons flowing. If the dissolved oxygen is removed from the electrolyte, either by bubbling N_2 or Ar through the solution or by pumping on the solution with a vacuum pump, illumination of the anode causes H_2 to be generated, but the short-circuit current decreases drastically so that the maximum value of η is only 1 to 2 percent for even the best TiO_2 anodes and 10 percent for $SrTiO_3$ anodes.

The transition from the photogalvanic mode of operation, in which current flows but no H_2 is generated, to the photoelectrolytic mode is readily understood in terms of the simplified energy diagram of a photoelectrolytic cell shown in Fig. III-1. (For simplicity, an acidic electrolyte has been chosen, but an entirely equivalent discussion could be given for a basic solution.) In this diagram, the Fermi level ξ_F for the anode and cathode is shown as coincident with $\xi(H^+/H_2)$. Consequently, photo-generated electrons supplied to the cathode via the external circuit are transferred to the H^+/H_2 level, causing the discharge of H_2 by the reaction



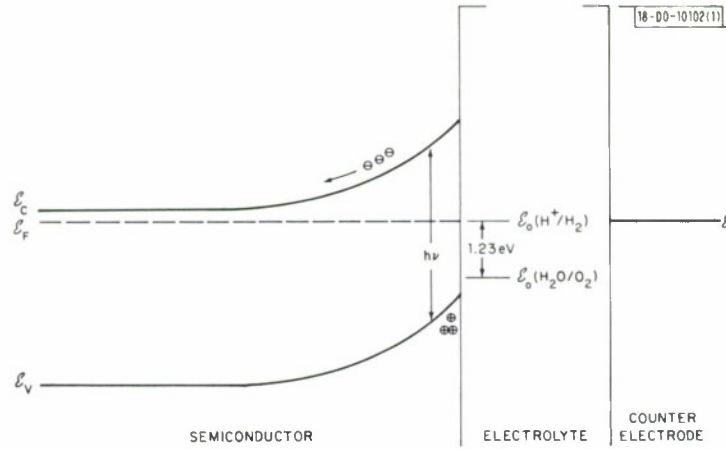


Fig. III-1. Energy diagram of photoelectrolytic cell with shorted electrodes.

while O_2 is formed at the anode by the reaction



If the electrolyte contains dissolved oxygen, however, the cathode approximates an oxygen electrode, so that ϵ_F actually lies quite far below $\epsilon(H^+/H_2)$ – specifically, by ~ 0.8 eV for pH = 0. In this case, the cell operates in the photogalvanic mode because it is energetically much more favorable for electrons to be transferred to the H_2O/O_2 level, causing the reduction of dissolved oxygen at the cathode by the reaction



than it is for them to be transferred to the $\epsilon(H^+/H_2)$ level according to Eq. (III-1). The very high values of η measured previously³ show that in the photogalvanic mode the electron-hole pairs generated by photon absorption are effectively separated by the band bending in TiO_2 , which is given by $b = \epsilon_F - (\epsilon_F)_{fb} \approx 0.8$ eV, where $(\epsilon_F)_{fb}$ is the flat-band potential. For TiO_2 at pH = 0, $(\epsilon_F)_{fb} \approx -0.2$ eV, relative to the standard calomel electrode. The value of b is even greater for $SrTiO_3$, for which we have measured $(\epsilon_F)_{fb} \approx -0.4$ eV, and the maximum values of η obtained for cells with $SrTiO_3$ anodes operating in the photogalvanic mode are similar to those obtained with TiO_2 . The high values of η also show that the oxygen overvoltage for charge transfer at the semiconductor-electrolyte interface is negligible for both TiO_2 and $SrTiO_3$ anodes when they are illuminated.

When the dissolved oxygen is removed from the electrolyte, it is no longer available for reduction according to Eq. (III-3). Therefore, the cell must operate in the photoelectrolytic mode since current flow now requires the discharge of H_2 at the cathode, according to Eq. (III-1), by the transfer of electrons from ϵ_F to the higher-lying H^+/H_2 level. Because of the energy barrier to this transfer, photo-generated electrons accumulate in the electrodes, raising ϵ_F (which must be the same for both electrodes, since they are shorted together). As ϵ_F rises, the band bending in the anode decreases, so that an increasing fraction of the photo-generated electron-hole pairs recombines instead of separating, causing a decrease in the rate at which electrons are transferred to the cathode via the external circuit. Simultaneously, the difference between ϵ_F and

$\epsilon(\text{H}^+/\text{H}_2)$ decreases, causing an increase in the rate of electron transfer from the cathode by the discharge of H_2 . When the two transfer rates become equal, there is no further accumulation of electrons, and a steady state is reached. With TiO_2 anodes, this occurs when ϵ_{F} is still 0.1 to 0.2 eV below $\epsilon(\text{H}^+/\text{H}_2)$, but the band bending is already so small that almost all the photo-generated pairs recombine. Thus, TiO_2 is quite different from the hypothetical semiconductor of the energy diagram in Fig. III-1, which exhibits significant band bending even when $\epsilon_{\text{F}} = \epsilon(\text{H}^+/\text{H}_2)$. For TiO_2 , $b \approx 0$ when $\epsilon_{\text{F}} = \epsilon(\text{H}^+/\text{H}_2)$, since $\epsilon(\text{H}^+/\text{H}_2) = -0.24$ eV at pH = 0 and is thus approximately equal to $(\epsilon_{\text{F}})_{\text{fb}}$ for TiO_2 . Even for SrTiO_3 anodes, which have a higher flatband potential, the band bending is only sufficient to yield maximum η values of 10 percent for photoelectrolytic cells with shorted electrodes, compared with 1 to 2 percent for cells using TiO_2 anodes.

Much greater efficiencies can be achieved for cells in which the electrodes are not shorted, so that the anode and cathode can have different Fermi levels. We have used several different experimental methods to keep $\epsilon_{\text{F}}(\text{anode})$ low enough for effective band bending, while keeping $\epsilon_{\text{F}}(\text{cathode})$ close enough to $\epsilon(\text{H}^+/\text{H}_2)$ for efficient transfer of electrons from the cathode. The simplest method is to apply an external bias voltage of a few tenths of a volt; less voltage is required with SrTiO_3 anodes than with TiO_2 anodes, because of the difference in flatband potential. The second method employs a photoelectrolysis cell with separate anode and cathode compartments that are filled respectively with strongly basic and strongly acidic solutions; the two compartments are connected by an agar bridge that allows the passage of ions yet does not permit mixing of the solutions. By using a similar procedure, Honda⁴ has obtained quantum efficiencies of ~ 10 percent for H_2 generation with TiO_2 anodes, and we have measured values in the same range. This method utilizes the electromotive force due to the difference in solution pH, $\epsilon = 0.059 \Delta[\text{pH}]$, to adjust the Fermi levels. The driving force is provided by the gradual neutralization of the acid and base solutions as the cell operates. Although it is necessary to supply the heat of neutralization, 15.9 kcal/mol, there is a considerable net gain in energy because the heat of combustion of H_2 is 68 kcal/mol. However, the method is somewhat inconvenient because it becomes less effective as the neutralization of the solutions causes $\Delta[\text{pH}]$ to decrease.

The third method we have used for adjusting the Fermi levels is to connect a photogalvanic cell in series with the photoelectrolytic cell. When the anodes of both cells are illuminated, the voltage produced by the photogalvanic cell is used to bias the photoelectrolytic cell. In experiments where both cells had TiO_2 anodes and platinized-Pt cathodes, we have obtained maximum η values of ~ 20 percent, computed on the basis of the total number of photons incident on the anodes of both cells.

None of these methods for adjusting the Fermi levels of the electrodes would be necessary if the band bending of the anode were sufficient for effective separation of the photo-generated electron-hole pairs even when $\epsilon_{\text{F}}(\text{anode}) = \epsilon(\text{H}^+/\text{H}_2)$. This implies a value of $(\epsilon_{\text{F}})_{\text{fb}}$ several tenths of a volt more negative than that of TiO_2 , and therefore an electron affinity less than that of TiO_2 by the same amount. Since the electron affinity of TiO_2 is ~ 4 eV, it follows that an ideal anode material for efficient photoelectrolysis should have an electron affinity no greater than ~ 3.5 eV. As pointed out previously,¹⁻⁴ for effective utilization of solar energy by means of photoelectrolysis it also will be necessary for the anode material to have an energy gap much less than that of TiO_2 , since only about 10 percent of the total solar energy reaching the earth is supplied by photons with energies exceeding 3.0 eV.

J. G. Mavroides	D. F. Kolesar
J. A. Kafalas	W. J. LaFleur
D. I. Tchernev	D. M. Tracy

B. CRYSTAL STRUCTURE OF $\text{KNdP}_4\text{O}_{12}$

Low-threshold, CW laser action previously has been reported in two compounds, $\text{NdP}_5\text{O}_{14}$ (Ref. 5) and $\text{NdLiP}_4\text{O}_{12}$ (Ref. 6), in which the Nd^{3+} ions are isolated from each other so that there is far less concentration quenching of the fluorescence lifetime than in conventional hosts such as Nd:YAG. The high Nd concentrations in these materials allow the operation of very small lasers, since efficient absorption of pump radiation occurs in short distances (50 to 100 μm), and the resulting optical gains can be quite large.

We recently have achieved CW laser action in two new high-Nd-concentration materials, $\text{NdAl}_3(\text{BO}_3)_4$ and $\text{KNdP}_4\text{O}_{12}$ (abbreviated as NAB and KNP, respectively). The laser properties will be described elsewhere, and the crystal structure of NAB has been reported previously.⁷ We now have determined the structure of KNP. Like NAB, KNP has an acentric space group, whereas both $\text{NdP}_5\text{O}_{14}$ and $\text{NdLiP}_4\text{O}_{12}$ are centrosymmetric. The lack of inversion symmetry is potentially advantageous for device applications, since it may allow second-order nonlinear optical processes (e.g., second-harmonic generation) as well as linear electro-optic modulation to be carried out directly in the laser crystals.

The reagents used in the growth of KNP crystals were Nd_2O_3 , K_2CO_3 , and $\text{NH}_4\text{H}_2\text{PO}_4$. A large excess of the latter two components was used as a flux. Typically, a mixture of the three compounds in a molar ratio of 1:3:12 (6.7, 8.3, and 27.6 g, respectively) was placed in a 100- cm^3 Au crucible, preheated at 200°C for 4 hours, and fired at 900°C overnight. The temperature then was reduced at 2°C/hour to 700°C and the furnace power was turned off. The crystals obtained by this procedure are typically platelets 0.05 to 0.03 mm thick and $0.5 \times 0.5 \text{ mm}^2$ in area. The broad faces of the platelets are either rectangular with (101) orientation, or hexagonal with $(\bar{1}01)$ orientation.

For x-ray diffraction studies, a cube-shaped crystal about 0.05 mm on a side was aligned along the b-axis. Oscillation and Weissenberg photographs showed diffraction symmetry $2/m$ and the systematic absence $0k0$, $k = 2n + 1$, consistent with space groups $\text{P}2_{1/m}$ and $\text{P}2_1$. Three-dimensional intensity data to $2\theta = 48^\circ$ were collected in the manner described previously.⁸ A total of 724 independent reflections was measured.

The heavy-atom method was used to solve the structure. A three-dimensional Patterson map showed only a strong peak close to $(1/2, 1/2, 1/2)$, which was assumed to be a Nd-Nd interaction. Initially the exact composition of the material was unknown, but because there was only one strong peak the number of Nd atoms per unit cell could not be greater than two. It was assumed that the two Nd atoms were occupying $2e$ of $\text{P}2_{1/m}$ or $2a$ of $\text{P}2_1$. A structure-factor calculation based on these positions gave a difference-function R value of 0.35 for both cases. A difference Fourier map based on this model gave unreasonable interatomic distances for $\text{P}2_{1/m}$, and it was concluded that there is no mirror plane perpendicular to the b-axis. This left $\text{P}2_1$ as the only possible space group, and it was possible to identify one independent K atom, four P atoms, and twelve O atoms in the unit cell. The final atom parameters, scale factor, and anisotropic temperature factors then were refined with a full-matrix least-squares program to give $R = 0.060$ and $R_w = 0.067$ for all reflections. The structure is monoclinic, with $a = 7.266(1) \text{ \AA}$, $b = 8.436(1) \text{ \AA}$, $c = 8.007(1) \text{ \AA}$, $\beta = 91.97(1)^\circ$, and $z = 2$. The concentration of Nd atoms is $4.08 \times 10^{21} \text{ cm}^{-3}$. The bond distances and angles are listed in Table III-1.

The structure of KNP is illustrated in Fig. III-2. The basic structural units are helical ribbons, $(\text{PO}_3)_n$, formed by corner-sharing of PO_4 tetrahedra. Therefore, this compound, like

TABLE III-1 BOND DISTANCES AND ANGLES FOR $\text{KNdP}_4\text{O}_{12}$			
	Distances (Å)		Angles (deg)
Dodecahedron Around Nd			
Nd - O(1)	2.47(2)		
Nd - O(4)	2.52(2)		
Nd - O(5)	2.53(2)		
Nd - O(6)	2.35(2)		
Nd - O(7)	2.43(2)		
Nd - O(10)	2.55(2)		
Nd - O(11)	2.46(2)		
Nd - O(12)	2.37(2)		
Irregular Shape Around K			
K - O(1)	2.81(2)		
K - O(4)	2.77(2)		
K - O(5)	2.85(2)		
K - O(6)	3.03(2)		
K - O(7)	2.94(2)		
K - O(10)	2.89(2)		
K - O(12)	2.81(2)		
Tetrahedron Around P(1)			
P(1) - O(1)	1.48(2)	O(1) - P(1) - O(2)	105(1)
P(1) - O(2)	1.59(2)	O(1) - P(1) - O(3)	106(1)
P(1) - O(3)	1.59(2)	O(1) - P(1) - O(11)	120(1)
P(1) - O(11)	1.38(2)	O(2) - P(1) - O(3)	106(1)
P(1) - P(2)	2.93(2)	O(2) - P(1) - O(11)	112(1)
P(1) - P(4)	3.06(2)	O(3) - P(1) - O(11)	106(1)
Tetrahedron Around P(2)			
P(2) - O(2)	1.58(2)	O(2) - P(2) - O(5)	113(1)
P(2) - O(5)	1.54(2)	O(2) - P(2) - O(6)	113(1)
P(2) - O(6)	1.50(2)	O(2) - P(2) - O(9)	98(1)
P(2) - O(9)	1.61(2)	O(5) - P(2) - O(6)	112(1)
		O(5) - P(2) - O(9)	114(1)
		O(6) - P(2) - O(9)	105(1)
Tetrahedron Around P(3)			
P(3) - O(8)	1.58(2)	O(8) - P(3) - O(9)	101(1)
P(3) - O(9)	1.56(2)	O(8) - P(3) - O(10)	108(1)
P(3) - O(10)	1.40(2)	O(8) - P(3) - O(12)	105(1)
P(3) - O(12)	1.53(2)	O(9) - P(3) - O(10)	109(1)
P(3) - P(2)	2.93(2)	O(9) - P(3) - O(12)	107(1)
P(3) - P(4)	2.89(2)	O(10) - P(3) - O(12)	124(1)
Tetrahedron Around P(4)			
P(4) - O(3)	1.60(2)	O(3) - P(4) - O(4)	109(1)
P(4) - O(4)	1.49(2)	O(3) - P(4) - O(7)	109(1)
P(4) - O(7)	1.48(2)	O(3) - P(4) - O(8)	101(1)
P(4) - O(8)	1.53(2)	O(4) - P(4) - O(7)	117(1)
		O(4) - P(4) - O(8)	110(1)
		O(7) - P(4) - O(8)	110(1)
Inter-tetrahedral Angles			
		P(1) - O(2) - P(2)	134(1)
		P(1) - O(3) - P(4)	147(1)
		P(2) - O(9) - P(3)	135(1)
		P(3) - O(8) - P(4)	136(1)

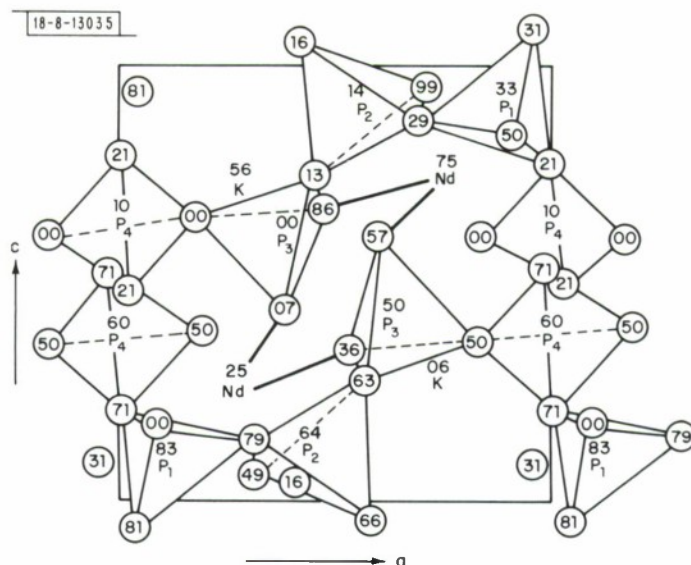


Fig. III-2. Crystal structure of $\text{KNdP}_4\text{O}_{12}$ (KNP) projected on a-c plane.

$\text{NdLiP}_4\text{O}_{12}$, should be designated as a metaphosphate. The ribbons (two per unit cell) run along the a-axis and are joined to each other by NdO_8 dodecahedra. The K-O bonds are weaker than either the Nd-O or P-O bonds, so the K atoms may be regarded as structural modifiers inserted into the $(\text{NdP}_4\text{O}_{12})^-$ network.

Each NdO_8 dodecahedron is surrounded by four others, with Nd-Nd distances of 6.661, 6.813, 6.910, and 7.057 Å, but the dodecahedra are isolated from each other in the sense that they do not share any O atoms. This type of isolation is the structural feature that is common to all the Nd compounds exhibiting reduced concentration quenching.⁹

Like $\text{NdP}_5\text{O}_{14}$, KNP is pseudo-orthorhombic. The deviation from orthorhombic symmetry is greater in KNP, with $\beta = 91.97^\circ$ compared with 90.48° in $\text{NdP}_5\text{O}_{14}$. Both compounds undergo a monoclinic-orthorhombic transition at elevated temperature. The transition temperature for KNP, which we have determined by differential thermal analysis, is 167°C , compared with 141°C for $\text{NdP}_5\text{O}_{14}$ (Ref. 10).

The Nd local-site configuration in KNP is illustrated in Fig. III-3, where it is seen that there is a distortion from two-fold symmetry, although the degree of acentricity is considerably less than

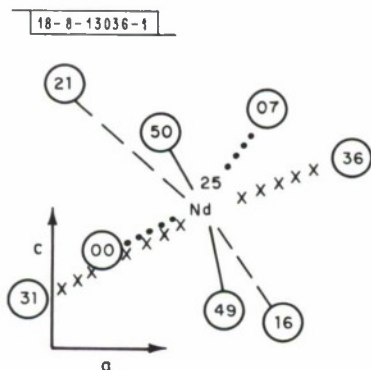


Fig. III-3. Local-site configuration of Nd in $\text{KNdP}_4\text{O}_{12}$.

it is for the Nd site in NAB.⁷ Consequently, the limiting lifetime for Nd⁺³ fluorescence at 1.06 μm is much higher in dilute $\text{KNd}_{1-x}\text{Gd}_x\text{P}_4\text{O}_{12}$ solid solutions than in $\text{Nd}_{1-x}\text{Gd}_x\text{Al}_3(\text{BO}_3)_4$ solutions, 275 μsec compared with 50 μsec (Ref. 11).

H. Y-P. Hong

C. ULTRAFAST GROWTH OF THIN GaAs LAYERS BY LIQUID-PHASE EPITAXY

The great majority of the multiple GaAs and $\text{Ga}_{1-x}\text{Al}_x\text{As}$ layers used to form double-heterostructure (DH) diode lasers are grown by liquid-phase epitaxy (LPE). In particular, they are prepared by the technique of equilibrium cooling, in which a Ga-rich growth solution saturated with As is placed in contact with a substrate wafer for a specified time while the system is being cooled at a uniform rate. The development of this technique has made it possible to grow smooth layers of uniform thickness (well below 1 μm , for the GaAs active layer) with controlled impurity concentration and Al content.

We recently reported¹² that even smoother LPE layers can be obtained if the growth solution is supercooled by about 5°C before being placed in contact with the substrate. We distinguished two different cases of this type, depending on whether the system temperature is reduced during the time of substrate-solution contact (supercooling technique) or is kept constant (step-cooling technique). It was shown experimentally that the thickness of the layers grown by both techniques, as well as by the equilibrium-cooling technique, was determined under the usual growth conditions by the amount of As that diffuses out of the growth solution to the substrate-solution interface.

The improvement in surface morphology resulting from the use of supercooled solutions is due to the effect of supercooling in increasing the uniformity with which growth is nucleated on the substrate. To study the nucleation process, we have been investigating the thickness and morphology of LPE layers obtained in extremely short growth times. This investigation has led to the development of a method for growing very thin layers of uniform and reproducible thickness at rates much faster than the highest that have been achieved by equilibrium cooling. These ultrafast rates may lead to an improvement in the reliability of DH diode lasers operating CW at room temperature, since it recently has been reported¹³ that the lifetimes of such lasers prepared by equilibrium cooling have been extended significantly by increasing the growth rate of the active region.

The procedure used for LPE growth is described in Ref. 14. Growth was carried out under flowing H_2 in a horizontal sliding graphite boat inside a resistance-heated furnace containing a heat pipe that eliminates any measurable temperature gradient along the entire length of the boat. The substrates were GaAs wafers oriented either (100) or 2° off (100). To facilitate measurement of the GaAs layer thickness, in each experiment a layer of $\text{Ga}_{0.67}\text{Al}_{0.33}\text{As}$ was first grown on the substrate, followed by the test layer of GaAs. A portion of the GaAs was removed by using a selective superoxol etchant,¹⁵ which etches GaAs about 40 times faster than $\text{Ga}_{0.67}\text{Al}_{0.33}\text{As}$. The GaAs layer thickness then was measured by using a two-beam interference microscope to determine the difference in height between the as-grown GaAs surface and the $\text{Ga}_{0.67}\text{Al}_{0.33}\text{As}$ surface exposed by etching.

Figure III-4 shows the thickness (d) of GaAs layers grown by the supercooling technique as a function of the amount of supercooling (Δ) of the growth solution in two series of experiments. The maximum and minimum values of d for each layer (1.1 cm^2) are indicated by error bars. In all cases, the solution and substrate were placed in contact at 800°C. In the first series of experiments, they were kept in contact for 12 sec. The value of d is seen to increase linearly

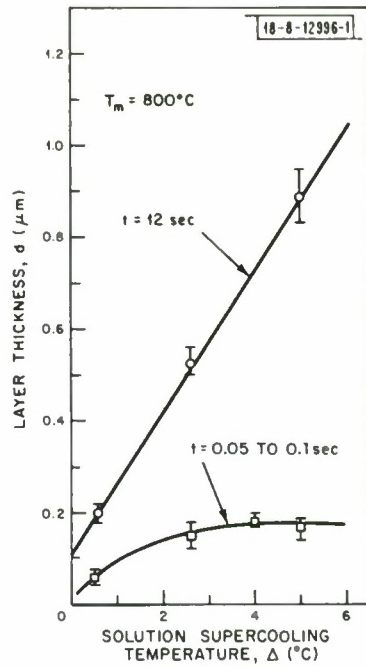


Fig. III-4. Variation of thickness (d) with amount of solution supercooling (Δ) for LPE GaAs layers grown by supercooling technique.

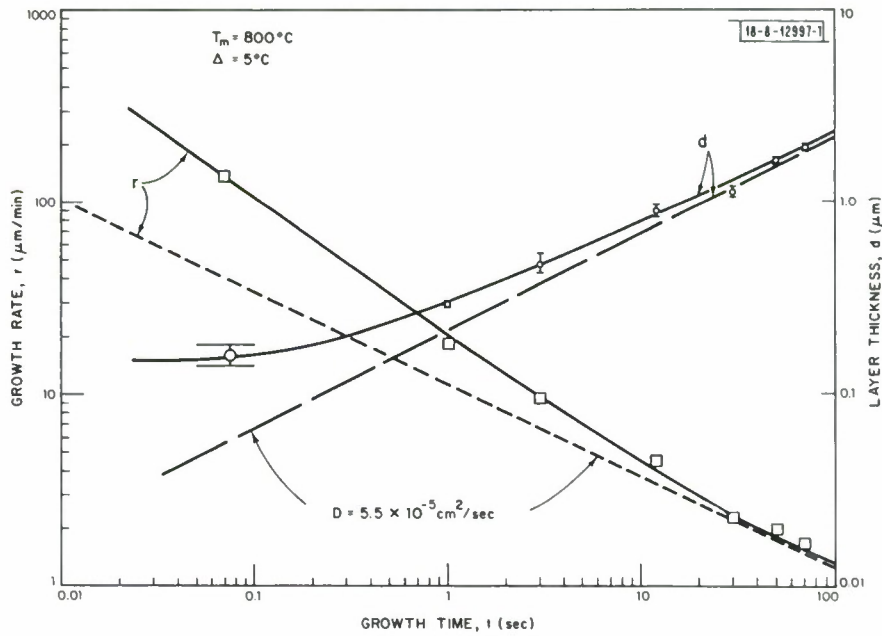


Fig. III-5. Variation of thickness (d) and growth rate (r) with growth time (t) for LPE GaAs layers grown by supercooling technique.

with Δ , as expected for diffusion-controlled growth. (The fact that the straight line through the data points does not extrapolate to $d = 0$ is due to transient effects at the beginning of growth.) The value of the diffusion constant D obtained by applying the equation for diffusion-controlled growth by the step-cooling technique [Eq. (1) of Ref. 12] to the experimental data is $5.5 \times 10^{-5} \text{ cm}^2/\text{sec}$, in good agreement with the values of 4 to $5 \times 10^{-5} \text{ cm}^2/\text{sec}$ obtained from various earlier data on LPE growth.¹²

In the second series of experiments for which data are plotted in Fig. III-4, the growth solution was pushed rapidly over the substrate without stopping. The push rate was 10 to 20 cm/sec, so that the time of contact between the solution and substrate was only 0.05 to 0.1 sec. All the layers grown in this way were extremely smooth and flat. In these experiments, the value of d initially increased as Δ increased but soon reached a limiting value of about $0.18 \text{ }\mu\text{m}$. This result indicates that growth by the fast-push technique is not diffusion-controlled. This conclusion is confirmed by the data shown in Fig. III-5, where d and the growth rate (r) are plotted as a function of growth time (t) for GaAs layers grown by the supercooling technique at 800°C with $\Delta = 5^\circ\text{C}$. (Even for the longest growth times, there was no significant change in the system temperature during the time the solution and substrate were in contact, so that the supercooling technique was actually equivalent to step-cooling.) At values of t approaching 100 sec, the measured values of d and r are in good agreement with those calculated (dashed lines) for diffusion-controlled growth with $D = 5.5 \times 10^{-5} \text{ cm}^2/\text{sec}$. At shorter times, however, d is significantly higher than the diffusion-controlled values, and for the growth time obtained with the fast-push technique, d hardly depends on t . Thus, the thickness of LPE layers grown by the fast-push technique does not depend strongly either on the growth time (i.e., on the push rate) or on the amount of supercooling. Therefore, the data of Figs. III-4 and III-5 indicate that layers of reproducible thickness should be obtained readily by this technique. Furthermore, it is seen in Fig. III-5 that the growth rate obtained by fast pushing exceeds $100 \text{ }\mu\text{m}/\text{min}$ (computed by assuming a growth time of 0.075 sec). To achieve growth rates this high by equilibrium cooling would require cooling rates of the order of $100^\circ\text{C}/\text{min}$.

The reproducibility of growth by the fast-push technique has been demonstrated by a series of experiments in which this method was used to grow the active layers for DH laser diodes on six different GaAs substrates. In each run, the growth temperature was 800°C and Δ was 5°C . The thickness values, which were measured with a scanning electron microscope after the wafers had been cleaved and etched with superoxol, were 0.099, 0.101, 0.137, 0.109, and $0.092 \text{ }\mu\text{m}$, and the thickness of each layer was uniform to within ± 5 percent. (The systematic difference of about $0.08 \text{ }\mu\text{m}$ between these values and the thickness of $0.18 \text{ }\mu\text{m}$ obtained for growth of GaAs on $\text{Ga}_{0.67}\text{Al}_{0.33}\text{As}$ in a single heterostructure configuration is due to the partial dissolution of the active layer during the growth of the second $\text{Ga}_{0.67}\text{Al}_{0.33}\text{As}$ barrier layer for the DH laser. This was confirmed by an experiment in which the active layer thickness was measured before and after the growth of the second barrier layer. The reduction in thickness was found to be $0.088 \text{ }\mu\text{m}$.)

J. J. Hsieh

REFERENCES

1. A. Fujishima and K. Honda, *Nature* 238, 37 (1972).
2. Solid State Research Report, Lincoln Laboratory, M.I.T. (1974:2), p. 32, DDC AD-783634/9.
3. *Loc. cit.* (1975:1), p. 35, DDC AD-A009848/3.
4. K. Honda, in Report of NSF/RANN Workshop, Boston University, 23-24 September 1974, p. 105.
5. H. G. Danielmeyer, G. Huber, W. W. Krühler, and J. P. Jeser, *Appl. Phys.* 2, 335 (1973).
6. K. Otsuka and T. Yamada, *Appl. Phys. Lett.* 26, 311 (1975); S. R. Chinn and H. Y-P. Hong, *Appl. Phys. Lett.* 26, 649 (1975).
7. Solid State Research Report, Lincoln Laboratory, M.I.T. (1974:4), p. 46, DDC AD-A004763/9; H. Y-P. Hong and K. Dwight, *Mater. Res. Bull.* 9, 1661 (1974), DDC AD-A006704/1.
8. H. Y-P. Hong, *Acta Crystallogr.* B30, 468 (1974), DDC AD-A000491/1.
9. H. Y-P. Hong and K. Dwight, *Mater. Res. Bull.* 9, 775 (1974), DDC AD-786294/9.
10. J. P. Budin, A. Milatos-Roufos, N. D. Chinh, and G. LeRoux, *J. Appl. Phys.* 46, 2867 (1975).
11. H. Y-P. Hong, *Mater. Res. Bull.* (to be published).
12. J. J. Hsieh, *J. Cryst. Growth* 27, 49 (1974), DDC AD-A008298/2.
13. M. Ettenberg and H. Kressel, *Appl. Phys. Lett.* 26, 478 (1975).
14. J. J. Hsieh and J. A. Rossi, *J. Appl. Phys.* 45, 1834 (1974), DDC AD-A000493/7.
15. R. A. Logan and F. K. Reinhart, *J. Appl. Phys.* 44, 4172 (1973).

IV. MICROELECTRONICS

A. CHARGE-COUPLED IMAGING ARRAYS

We have completed the fabrication of a two-phase buried channel 100×1 charge-coupled imaging device which has been described previously,¹ and have successfully operated the device in a four-phase buried-channel mode. The current devices have had an ion-implanted barrier placed under alternate gates to create true two-phase operation.

The structure is similar to that described by Erb *et al.*² using two levels of polysilicon to form overlapping gates on a gate insulator of uniform thickness [Fig. IV-1(a-c)]. The complete fabrication process is as follows: After the p^+ channel stop and n^+ diode diffusions are completed, the channel area is opened and phosphorous atoms are implanted at 100 keV into the 30- to 50-ohm-cm p-type substrate at a dose level of $1.5 \times 10^{12} \text{ cm}^{-2}$. Subsequently a 1000-Å gate oxide is grown, 500 Å of Si_3N_4 is deposited, and the first-level polysilicon layer is deposited and doped by phosphorous diffusion. The first-level (storage) gates are etched to a nominal length of 8.9 μm , leaving 6.4 μm between gates. The barrier implant is then made using 90-keV boron atoms at a dose level of $8 \times 10^{11} \text{ cm}^{-2}$. The first-level polysilicon in this case functions as an implantation mask, insuring that the boron implant is self-aligned. After the first-level gates are oxidized, the second level of polysilicon is deposited, doped, and etched to produce the transfer gates [Fig. IV-1(b)]. The choice of polysilicon for both levels was made so that the device would have maximum sensitivity to frontside illumination for the intended imaging application. Figure IV-1(c) illustrates qualitatively the asymmetric channel potential created by this structure for the case where the pair of electrodes labeled ϕ_1 are at a low potential, and the pair labeled ϕ_2 are at a high potential.

Measurements of the channel potential vs gate voltage for a typical device are shown in Fig. IV-2. The data were obtained by measuring the threshold gate voltage for conduction between input and output diodes (described fully elsewhere¹) for various values of diode-to-substrate reverse bias. The potential well under the storage gates at zero gate bias has been found to be 5.3 to 5.5 V greater than that under the transfer gates. Calculations predict a potential difference of 5.8 V, of which 5.3 V are due to the space charge of the boron and 0.5 V to the work function difference between the n^+ gates and the n and p silicon surfaces. This agrees well with the measurement and indicates that almost all the boron penetrated the gate insulator and was activated by subsequent high-temperature processing. The maximum charge-handling capability, that is the amount of charge that can be stored under the storage gates without spilling over to the adjoining transfer gates, has been calculated numerically for the measured barrier height and is found to be 750,000 electrons compared with a measured value of 620,000 electrons. The calculated value takes account of the lateral diffusion of the p^+ channel stop of 3.2 μm , reducing the channel width from 25.4 to 19.0 μm . However, it does not take into account the influence of the neighboring electrodes in reducing the potential at the periphery of the well and therefore reducing the effective storage area. This "edge effect" may account for most of the discrepancy.

Measurements of transfer inefficiency at room temperature have been made at a clock frequency of 1 MHz and found to be $1.3 \pm 0.5 \times 10^{-4}$ per transfer. This value is still higher than the best values of about 1×10^{-5} obtained for buried channel operation.³ Room-temperature dark-current values were in excess of 300 nA/cm², indicating the presence of a rather large

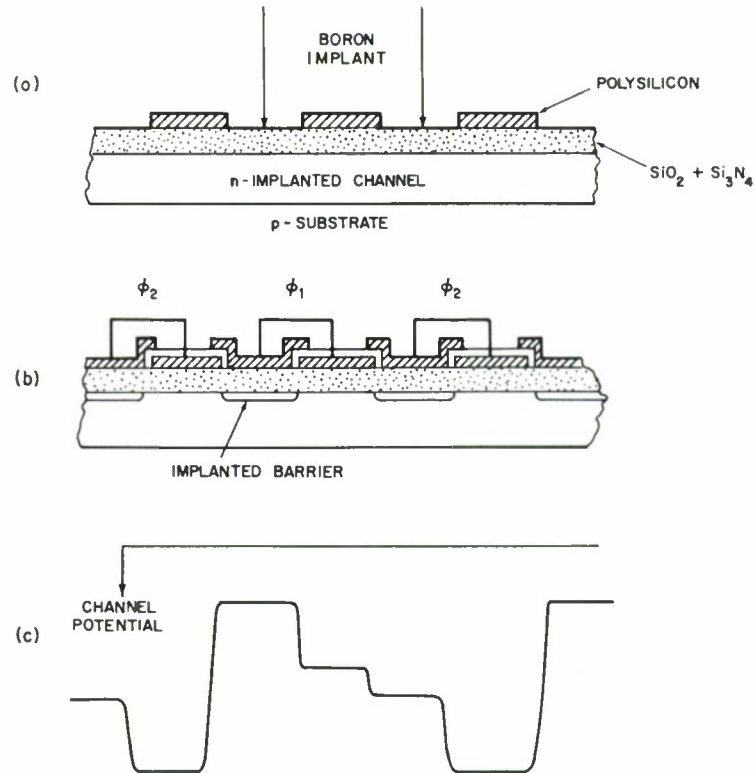


Fig. IV-1. Two-phase overlapping gate CCD (a) after first-level polysilicon has been deposited and etched, and (b) after boron barrier implant and second-level polysilicon deposition and definition. Pairs of electrodes from two levels are alternately connected as two phases, ϕ_1 and ϕ_2 . Asymmetric channel potential in this device is depicted in (c) for case where ϕ_1 is at low and ϕ_2 is at high potential.

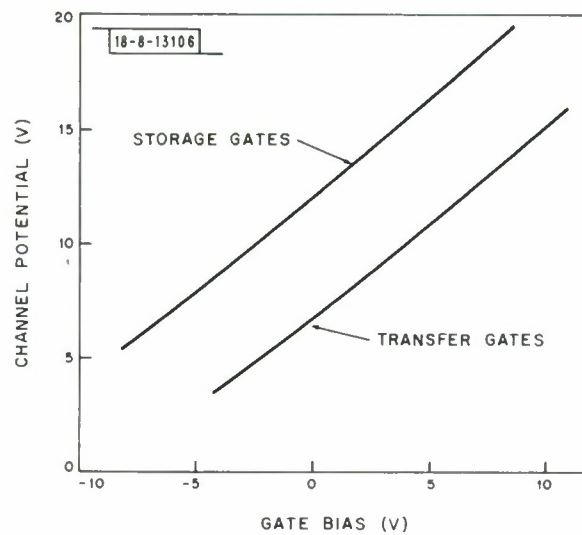


Fig. IV-2. Measurements of channel potential vs gate bias (substrate grounded) for storage gates (first-level polysilicon) and transfer gates (second-level polysilicon).

density of deep levels. Such levels can serve as trapping centers and may account for the transfer loss. Efforts currently are being directed at achieving low dark currents in the finished devices.

B. E. Burke R. W. Mountain
R. A. Cohen W. H. McGonagle

B. PACKAGING CIRCUITS FOR K_a -BAND PARAMETRIC AMPLIFIERS

Varactor diodes currently are being fabricated for use in a K_a -band parametric amplifier which will be used in a ground-station receiver for the LES-8/9 satellite program. These diodes have been characterized extensively by Deloach and network analyzer measurements,⁴ and have been found to be of sufficiently high quality to make parametric amplifiers with the required properties. Current efforts in this program have been concentrated on developing a packaging network which provides contact between the diode and the waveguide circuit.

A parametric amplifier circuit consists not only of external circuit elements but also the diode package. The circuit should provide efficient coupling between the pump source and the diode and present a series resonance to the diode at the idler frequency, as well as transforming the negative impedance of the pumped varactor to the level required to obtain the necessary reflection amplifier gain. It is desirable to perform as many of these circuit functions as possible within the packaging network because the lower Q's of lumped parameter networks result in wider operating bandwidths. A further consideration is that the various circuit components should be as lossless as possible, and should be mechanically strong and reliable. The design considerations for two alternative packaging schemes are discussed below, and the characteristics of each are presented.

The first approach is based on the use of a single capacitive standoff which is connected to the device by an inductive ribbon [Fig. IV-3(a)]. It is impossible to thermocompression (TC) bond the ribbon directly to the small (8 μ m) diodes being used, and, consequently, a lead must be fabricated as part of the device. In the packaging operation, the inductive ribbon is TC bonded to the fabricated lead and used to lift the lead up from the GaAs surface. The ribbon is then TC bonded to a metalized quartz post as shown. Figure IV-3(b) shows the electrical equivalent network of this packaging arrangement. Efficient pump coupling can be obtained if the loop consisting of the post capacitance, the lead inductance, and the varactor diode is resonant at the pump frequency. Also, the condition necessary for proper idler termination when the waveguide circuit is designed to present a series resonance at the idler frequency is that the lead inductance be resonated against the diode capacitance. If a signal frequency of 37.5 GHz, a pump frequency of 102.5 GHz, and an average device capacitance of 0.04 pF is assumed, the lead inductance (L_1) and post capacitance (C_1) can be calculated. These values are determined uniquely as 0.15 nH and 0.027 pF, respectively, and yield a calculated output impedance at the signal frequency with a resistive component of -11.8 ohms and a reactive component of -50.1 ohms.

The primary advantage of this packaging approach is its simplicity. The circuit can be analyzed easily, and the element values at RF frequencies (which may differ considerably from lower frequency values) can be measured with comparative ease. Moreover, this general approach has been used successfully by other workers in parametric amplifier design at K_a -band.⁵ However, this approach does suffer from several disadvantages. C_1 and L_1 are small and difficult values to achieve, and this results in a structure which is fragile and hard to fabricate. Also, the simplicity in packaging circuit topology is exchanged for greater complexity in the external microwave circuitry which must participate in the termination of the idler frequency,

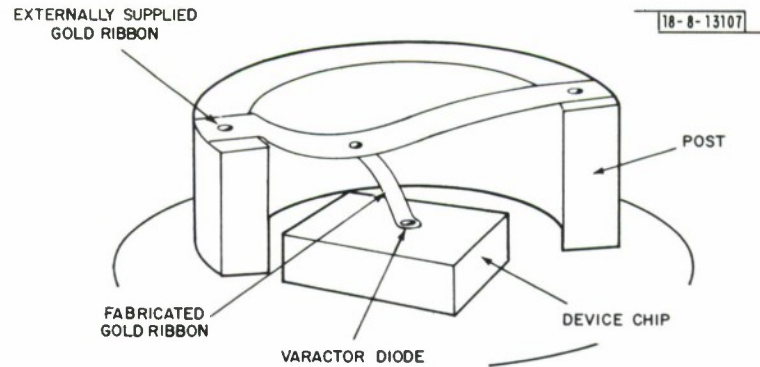


Fig. IV-3(a). Drawing of single-standoff, varactor-diode packaging approach showing inductive ribbon TC bonded to metalized post and fabricated device lead.

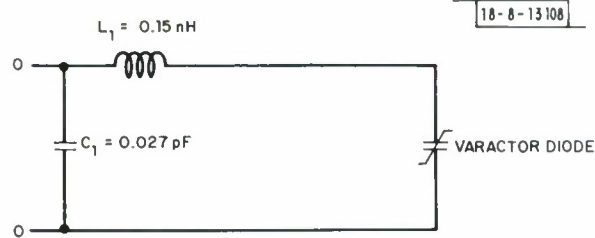


Fig. IV-3(b) Electrical equivalent network giving calculated required values for lead inductance (L_1) and post capacitance (C_1) for signal frequency of 37.5 GHz, pump frequency of 102.5 GHz, and average diode capacitance of 0.04 pF.

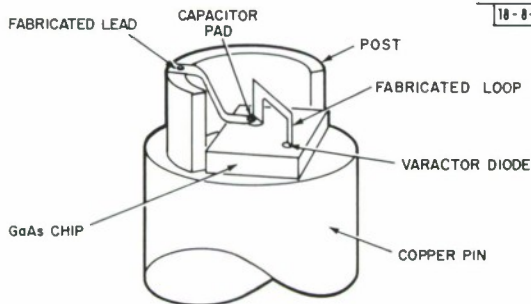


Fig. IV-4(a). Drawing of fabricated, inductive-loop packaging approach showing inductive loop raised off surface of GaAs, and lead picked up and bonded to metalized post.

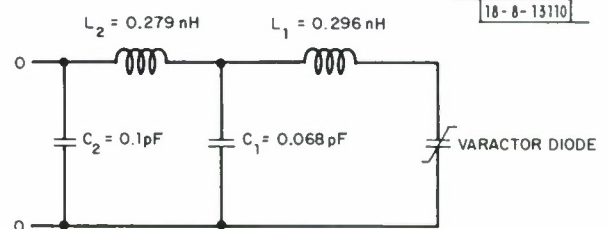


Fig. IV-4(b). Electrical equivalent network showing possible set of values for lead inductance (L_2), fabricated loop inductance (L_1), pad capacitance (C_1), and post capacitance (C_2), which would provide suitable signal frequency impedance transformation and series resonate device at idler frequency.

operate at a very low impedance level, and tune out the substantial reactive impedance at the signal frequency. Further, since the idler frequency is not completely terminated within the packaging elements, narrower bandwidths will result.

A number of devices have been fabricated and packaged in this manner. An idler resonance of 62 GHz and a pump resonance of 97 GHz have been measured for one packaged device with a diode having a capacitance of 0.035 pF. A degenerate parametric amplifier also has been fabricated using another device whose pump resonance was at 73 GHz. The measured gain was 2.5 dB. Current development efforts center upon repeatedly achieving the required packaging circuit elements and in fabricating signal frequency guiding structures of impedance levels low enough to provide adequate gain.

The second packaging approach is based on an inductive loop and a capacitive pad which are fabricated as an integral part of the chip. This scheme is illustrated in Fig. IV-4(a). The varactor diode is connected to the capacitive pad through the inductive loop which is mechanically bent up during the packaging process. The capacitive pad is fabricated over proton-bombarded, high-resistivity GaAs which is the capacitor dielectric in this case. A lead is also fabricated as part of the device, and shares the connection to the capacitive pad. This lead is sufficiently long to be attached to the capacitive post as shown in Fig. IV-4(a).

The electrical equivalent network of this arrangement is shown in Fig. IV-4(b). Qualitatively, this network differs from that discussed earlier in that an additional ladder network stage has been added comprised of the lead inductance L_2 and the post capacitance C_2 . The present design uses the greater number of degrees of freedom offered by this circuit to provide both a suitable signal frequency impedance transformation, and to series resonate the device at the idler frequency. It is not possible to achieve these conditions and also provide a resonance at the pump frequency. However, it should be possible to inductively couple to the loop in the absence of a resonance. One possible set of circuit element values is shown in Fig. IV-4(b) which results in a purely real calculated output impedance of -164 ohms.

Most of the advantages of this arrangement over that discussed above derive from its greater flexibility. Terminating the idler frequencies entirely within the packaging network results in wider bandwidths and eliminates the need for an external idler cavity. Moreover, a low-impedance guiding structure is not needed at the signal frequency because the impedance transformation is performed by the packaging network. Another advantage of this design is that the element values can be much more readily realized. The required post capacitance of 0.1 pF can, for example, be fabricated from alumina instead of quartz. The loop and lead required will fit onto a 20-mil chip, and the diameter of the capacitive pad required is approximately 1 mil, a quite convenient size.

The disadvantages of this arrangement very nearly mirror the advantages of the simpler approach. The greater complexity of this circuit requires that considerably more sophisticated measuring techniques be used to determine actual parameter values at RF frequencies. Moreover, pumping the device requires some external tuning because of the lack of resonance at the pump frequency.

A number of varactor diodes have been packaged in this manner. A scanning electron micrograph of a structure is shown in Fig. IV-5. Extensive network analyzer measurements have verified that, with minor modifications to the post reactance,⁶ the circuit of Fig. IV-4(b) describes the electrical behavior of this configuration at the signal frequency.

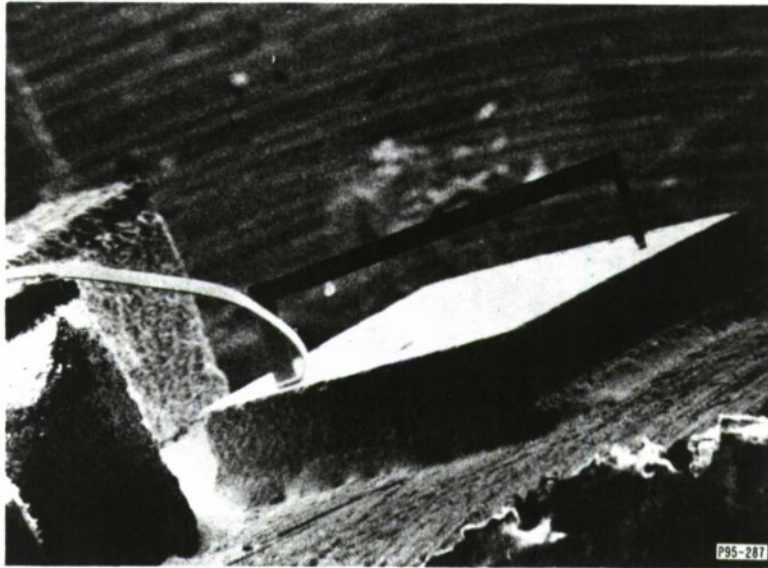


Fig. IV-5. Scanning electron micrograph of fabricated, inductive-loop device showing raised loop and lead bonded to metalized post.

In order to test whether the idler frequencies are being properly terminated by this structure, a tripler has been constructed out of this device. The tripler has operated successfully between 35 and 105 GHz, indicating an idler resonance at 70 GHz. However, some difficulty has been encountered in pumping the device, as expected. Present efforts in this area center upon fabricating waveguide circuits which will promote inductive coupling to the loop.

R. A. Murphy G. B. Berk (Group 66)
W. T. Lindley B. C. Clifton (Group 63)

REFERENCES

1. Solid State Research Report, Lincoln Laboratory, M.I.T. (1974:4), p. 55, DDC AD-A004763/9.
2. D. M. Erb, W. Kotyczka, S. C. Su, C. Wang, and G. Clough, IEEE International Electron Devices Meeting, Session 2, Washington, D.C., 3-5 December 1973.
3. R. W. Broderson, Texas Instruments, Dallas, Texas, private communication.
4. Solid State Research Report, Lincoln Laboratory, M.I.T. (1975:1), p. 11, DDC AD-A009848/3.
5. J. A. Calviello, P. R. Liegey, and C. Smilowitz, Proc. IEEE (Letters) 59, 419 (1971).
6. W. J. Getsinger, IEEE Trans. Microwave Theory Tech. MTT-14, 58 (1966), DDC AD-641005.

UNCLASSIFIED

SECURITY CLASSIFICATION OF THIS PAGE (When Data Entered)

REPORT DOCUMENTATION PAGE		READ INSTRUCTIONS BEFORE COMPLETING FORM
1. REPORT NUMBER ESD-TR-75-249	2. GOVT ACCESSION NO.	3. RECIPIENT'S CATALOG NUMBER
4. TITLE (and Subtitle) Solid State Research		5. TYPE OF REPORT & PERIOD COVERED Quarterly Technical Summary, 1 May - 31 July 1975
		6. PERFORMING ORG. REPORT NUMBER 1975:3
7. AUTHOR(s) McWhorter, Alan L.		8. CONTRACT OR GRANT NUMBER(s) F19628-76-C-0002
9. PERFORMING ORGANIZATION NAME AND ADDRESS Lincoln Laboratory, M.I.T. P.O. Box 73 Lexington, MA 02173		10. PROGRAM ELEMENT, PROJECT, TASK AREA & WORK UNIT NUMBERS Project No. 649L
11. CONTROLLING OFFICE NAME AND ADDRESS Air Force Systems Command, USAF Andrews AFB Washington, DC 20331		12. REPORT DATE 15 August 1975
		13. NUMBER OF PAGES 64
14. MONITORING AGENCY NAME & ADDRESS (if different from Controlling Office) Electronic Systems Division Hanscom AFB Bedford, MA 01731		15. SECURITY CLASS. (of this report) Unclassified
		15a. DECLASSIFICATION DOWNGRADING SCHEDULE
16. DISTRIBUTION STATEMENT (of this Report) Approved for public release; distribution unlimited.		
17. DISTRIBUTION STATEMENT (of the abstract entered in Block 20, if different from Report)		
18. SUPPLEMENTARY NOTES None		
19. KEY WORDS (Continue on reverse side if necessary and identify by block number)		
solid state devices quantum electronics materials research microelectronics	photodiode devices lasers laser spectroscopy	infrared imaging imaging arrays surface wave transducers
20. ABSTRACT (Continue on reverse side if necessary and identify by block number)		
<p>This report covers in detail the solid state research work of the Solid State Division at Lincoln Laboratory for the period 1 May through 31 July 1975. The topics covered are Solid State Device Research, Quantum Electronics, Materials Research, and Microelectronics. The Microsound work is sponsored by BMDATC and is reported under that program.</p>		

UNCLASSIFIED

SECURITY CLASSIFICATION OF THIS PAGE (When Data Entered)